Three Regimes of Internal Gravity Wave–Stable Vortex Interaction Classified by a Nondimensional Parameter δ: Scattering, Wheel-Trapping, and Spiral-Trapping with Vortex Deformation

KAORU ITO[a] AND TOMOHIRO NAKAMURA[a]

[a] *Pan-Okhotsk Research Center, Institute of Low Temperature Science, Hokkaido University, Sapporo, Japan*

(Manuscript received 6 January 2022, in final form 20 December 2022)

ABSTRACT: The internal wave–vortex interaction was investigated for a broad parameter range except near inertial waves, by 1) scaling, 2) numerical experiments, and 3) the estimation of possible occurrences. By scaling, we identified a nondimensional parameter, $\delta = (V/c)[1/(kR)]$, where V is the vortex flow speed, R is the radius, c is the incident wave phase speed, and k is the horizontal wavenumber. As δ appears in all terms related to the interaction, it is important in the classification of the wave–vortex interaction. Numerical experiments were conducted on internal waves incident on a stable barotropic vortex with a parameter range of $\delta = [0.001, 1.7]$, which is much broader than that used in previous studies ($\delta \ll 1$). We found new phenomena for $\delta > 0.15$, in addition to previously known scattering for $\delta \leq 0.15$ (scattering regime). For $0.15 < \delta \leq 0.4$, part of the incident internal wave is trapped in a vortex, forming a wheel-like shape maintaining a superinertial frequency (wheel-trapping regime). When $\delta > 0.4$, incident waves are trapped, but with a spiral shape (spiral-trapping regime). Spiral-shaped trapped waves release momentum by wave breaking, which deforms the vortex into a zigzag shape in the vertical direction. Vortex deformation produces vertical shear, which rapidly increases the vertical wavenumber of the incident wave. The distribution of δ in the Pacific Ocean was estimated using a high-resolution (1/30°) ocean general circulation model output. We found the occurrences of all three regimes. The scattering and wheel-trapping regimes are distributed broadly and varied seasonally, thus affecting mixing variability.

SIGNIFICANCE STATEMENT: Oceanic internal waves constitute the fundamental forcing of overturning and material circulation, because internal waves eventually break and cause vertical mixing. Interactions between internal waves and vortices affect wave properties and, therefore, mixing. However, as far as we are aware, all previous studies have focused on large weak vortices relative to waves. Here, we investigated such interactions for a much larger parameter space and identified two new regimes, in which vertical mixing is caused by newly found internal wave trapping and vortex deformation processes. We identified a nondimensional parameter that classifies the regimes and estimated their spatiotemporal distribution. These results suggest new energy routes from internal waves to turbulence and are applicable to other types of waves and vortices.

KEYWORDS: Eddies; Internal waves; Mixing; Nonlinear dynamics; Wave breaking; Numerical analysis/modeling

1. Introduction

The breaking and dissipation of internal waves are a major energy source for vertical mixing in the oceans, playing a crucial role in thermohaline and material circulation and the ecosystem. Understanding vertical mixing requires understanding internal wave propagation and dissipation.

The interaction between internal waves and a vortex is one of the processes that control the internal wave field and dissipation (mixing). This is because internal waves propagate over long distances and are likely to encounter a vortex, and the interaction affects wave propagation and properties. Although part of the internal waves generated by tides breaks and dissipates in the vicinity of the generation areas (Polzin et al. 1997; Klymak et al. 2008; Nakamura et al. 2010), a large part of the generated wave energy (particularly for low vertical modes) propagates far from the generation areas (St. Laurent et al. 2002; Rudnick et al. 2003; Alford 2003). These low modes are expected to encounter vortices, as low-vertical-mode internal waves propagate over long distances (Ray and Mitchum 1997; Ray and Cartwright 2001), and because vortices are prevalent in the oceans (Chelton et al. 2011).

When internal waves are incident on a vortex from its side, the interaction affects the wave propagation, phase, amplitude, wavenumber, and the field and dissipation of internal waves. These effects occur through refraction (Kunze 1985; Rainville and Pinkel 2006; Godoy-Diana et al. 2006; Chavanne et al. 2010; Duda et al. 2018; Lelong et al. 2020), wave capture (Jones 1969; Badulin and Shrira 1993; Bühler and McIntyre 1998, 2005; Moulin and Flór 2005; Polzin 2010), weakly nonlinear three-wave resonance (Warn 1986; Dong and Yeh 1988; Lelong and Riley 1991; Bartello 1995; Ward and Dewar 2010), beam-like scattering (Dunphy and Lamb 2014; Dunphy et al. 2017), interaction with geostrophic flow through the mechanism described by Young and Ben-Jelloul (1997, hereafter YBJ) and its line (Klein and Smith 2001; Xie and Vanneste 2015; Wagner and Young 2015; Salmon 2016; Wagner et al. 2017), and scattering quantified by an equation of wave phase–space energy density (Danioux and Vanneste 2016; Savva and Vanneste 2018; Kafiabad et al. 2019; Dong et al. 2020; Savva et al. 2021, hereafter, SKV).

Corresponding author: Kaoru Ito, k-ito@lowtem.hokudai.ac.jp

DOI: 10.1175/JPO-D-21-0309.1

The internal wave–vortex interaction is also important for practical purposes. These include the evaluation of the nonstationarity of internal tides, which affects the detection of internal tides in sea surface height obtained by satellite altimeters, predicting in situ internal tides (Ray and Zaron 2011; Shriver et al. 2014; Zaron and Egbert 2014), analysis of upcoming satellite altimetry, Surface Water and Ocean Topography (SWOT; Fu and Ferrari 2008), Coastal and Ocean Measurement mission with Precise and Innovative Radar Altimeter (COMPIRA; Uematsu et al. 2013), and separation of wave (fast) modes from vortical (slow or geostrophic) modes for dynamical analysis and numerical forecasting (Hoskins et al. 1978; Leith 1980).

However, previous studies have focused on interactions with weak and/or large eddies relative to internal waves, and thus, interactions remain uninvestigated for relatively strong and/or small eddies. Furthermore, estimates of the distribution and temporal variation in the internal wave–vortex interaction remain limited to small areas. Here, we investigated the internal wave–vortex interaction in a broad parameter range, focusing on internal waves incident on a vortex except for near-inertial waves, and we estimated the distribution and seasonal variation of such interactions. The remainder of this section discusses the above points more specifically with the help of the present results.

Many wave–vortex interactions occurring in the oceans fall outside the parameter range investigated in previous studies, particularly for small, strong eddies (i.e., $R_o \gtrsim 1$, $F_r \gtrsim 1$, $kR < 1$, where, R_o is the Rossby number, F_r is the Froude number, k is the incident wavenumber, and R is the vortex radius). To the best of our knowledge, all theoretical studies have made one or both of the following assumptions. The first assumption is $R_o \ll 1$ or $F_r \ll 1$, where R_o or F_r is used to scale the governing equations. The second is regarding the ratio of the wave and vortex length scales kR. The ratio is assumed to be $kR \gg 1$ in the WKB-type approach (e.g., ray tracing) and $kR \sim 1$ in weak nonlinear interaction theories. The YBJ model also assumes $kR \sim 1$ implicitly through the use of a single horizontal length scale, though Xie and Vanneste (2015) suggested kR can be $\ll 1$ in the YBJ model provided that near inertial waves have larger (or similar) vertical length scale than a geostrophic flow. The exceptions are those that utilize the Wigner transform (e.g., SKV), which enables no assumption on kR.

However, in the real oceans, cases with a parameter range of R_o, $F_r \gtrsim 1$ or $kR < 1$ frequently occur (e.g., Calil et al. 2008; Nakamura et al. 2012). First, the case $R_o \sim 1$ or $F_r \sim 1$ occurs for strong vortices. Second, $kR < 1$ occurs because internal waves have wavelengths of a few hundred kilometers for the first vertical mode in deep basins, whereas submesoscale or mesoscale eddies have diameters of a few kilometers to some hundred kilometers. In other words, it can occur when waves and vortices are dominated by different vertical modes or vortices are not in the geostrophic balance. Several numerical studies have investigated somewhat broader ranges of parameters with larger R_o or F_r than those used in theoretical studies (Kuo and Polvani 1999; Dewar and Killworth 1995; Farge and Sadourny 1989; Dunphy and Lamb 2014; Ansong et al. 2015; Ponte and Klein 2015; Kerry et al. 2014; Kelly et al. 2016; Dunphy et al. 2017). However, the broad parameter range remains unknown.

Therefore, we conducted numerical experiments on the interaction of internal waves incident on a stable barotropic vortex from its side in a much broader parameter range compared with previous studies. We varied both the major nondimensional parameters (kR, R_o, F_r) and relevant dimensional parameters (V_0, R, c, k, and N), as described in section 2. Here, $F_r \equiv V_0/c$ and $R_o \equiv V_0/(fR)$, where V_0, c, N, f are the maximum vortex flow speed, phase speed of the incident waves, buoyancy frequency, and Coriolis parameter, respectively. We employed all parameters, as it was not clear which nondimensional parameter would be useful for scaling the wave–vortex interaction in such a broad parameter range, if any.

From the experiments, we identified a nondimensional parameter $\delta \equiv (V_o/c)[1/(kR)]$ that classifies wave responses to a vortex into three types; two new types in the parameter range that have not been explored previously, in addition to the already known scattering type (section 4). The parameter δ is theoretically supported by scaling idealized governing equations (section 3). Parameter δ appears in all terms that are the product of the wave and vortex variables. Accordingly, as δ increases, the nonlinearity or the interaction becomes stronger. When $\delta \ll 1$, known scattering occurs.

Viewed in terms of δ, previous studies have not investigated the range $\delta \gtrsim 1$, although this can occur in the oceans. The WKB-type approach implicitly assumes $\delta \ll 1$ by assuming both the separation of spatial scales, which requires $1/(kR) \ll 1$ and a quasi-linear approximation, in which waves are nearly sinusoidal and, therefore, require $F_r \ll 1$. With the two assumptions combined, it follows that $\delta \ll 1$, because $\delta = F_r/(kR) \ll F_r \ll 1$. Similarly, weakly nonlinear interaction theories implicitly assume $\delta \ll 1$ through the assumptions that $F_r \ll 1$ or $R_o \ll 1$ and that the horizontal scales of waves and vortices are of the same order ($kR \sim 1$). This is because if $F_r \ll 1$, $\delta = F_r/(kR) \sim F_r \ll 1$, and because if $R_o \ll 1$, $\delta = R_o(f/\omega) < R_o \ll 1$ (because $f < \omega$), where ω is incident wave frequency. Note the last inequality implies $\delta \ll 1$ if $R_o \ll 1$. It follows that theories in agreement with YBJ and/or SKV implicitly assume $\delta \ll 1$. Although the YBJ equation could cover $\delta \sim 1$ provided $R_o \sim 1$, the governing equations become intractable, which is one of the reasons we used a numerical model.

Moreover, $\delta \ll 1$ in almost all previous numerical experiments; otherwise, δ cannot be specified as one or more of k, c, R, and V is not specified, although descriptions and/or figures suggest that the results are in the known scattering regime (i.e., $\delta \ll 1$). Dunphy and Lamb (2014) examined a fairly broad parameter range. Nevertheless, the phenomena found in the regimes of $\delta \lesssim 1$ were not described, probably because their focus was on the properties of the waves leaving the vortex. We investigated a broader range (δ = [0.001, 1.7]) and focused on waves captured in the vortex. Dunphy et al. (2017) focused on the case $\delta \ll 1$, although a coefficient corresponding to δ was listed as one of the coefficients of nonlinear terms (δ corresponds to their $R/\tilde{\omega}$). Bartello (1995) explored a broad range (R_o, F_r = 0.1 to 100) but focused only on the time evolution of the ratio of nongeostrophic to geostrophic energies (geostrophic adjustment) and not on wave response.

Brunner-Suzuki et al. (2012, 2014) conducted experiments with δ of ~0.13 ($R_o = 0.15$) and obtained an interesting result; that is, waves promote the deformation of a vortex, called an *S* vortex, to a dipole vortex. However, this process differs completely from that investigated here, as their vortices are unstable. Observations have been reported for the case $\delta \ll 1$ (e.g., Huang et al. 2018), but not for the case $\delta \gtrsim 1$.

Apart from the dynamics, the distribution, frequency, and variability of wave–vortex interactions in the oceans remain unclear, as previous studies have been based on theoretical analyses or numerical experiments with ideal settings. Although some simulations have simultaneously calculated vortices and tides, their interaction has not been examined (Arbic et al. 2010, 2012). Therefore, we investigated whether the newly found interactions and the resulting mixing could occur in the real oceans and identified where and when the interactions of each regime occur. To this end, we calculated the approximate distribution of and seasonal variation in δ in the Pacific Ocean to estimate the possible occurrence, strength, and variability of wave–vortex interactions.

The remainder of this paper is organized as follows. Section 2 describes the methods. Section 3 introduces δ by scaling. The results of numerical experiments are shown in section 4. An estimate of δ is presented in section 5. The results are summarized and discussed in section 6.

2. Methods

This section focuses on three topics. Section 2a describes the problems considered in scaling in section 3 and numerical experiments in section 4. Section 2b describes the settings of the numerical experiments and model, followed by the estimation methods of the trapping rate of wave energy in a vortex and increase rate of the vertical wavenumber in section 4. Finally, section 2c describes the estimation method of the nondimensional parameter δ in section 5, which is argued in sections 3 and 4.

a. *Problems considered in scaling and numerical experiments*

We considered the interaction between the vortex and internal waves incident from the side (Fig. 1). The initial vortex was balanced dynamically, and the incident waves were monochromatic with a vertical mode structure. Although the numerical experiments allow three-dimensional, strongly nonlinear interactions, the scaling adopts shallow water equations for simplicity, as the vertical structure would have a secondary importance until it is changed by such nonlinear interactions.

b. *Numerical experiments*

1) SETTINGS OF NUMERICAL EXPERIMENTS

The initial vortices were idealized as barotropic to focus on the effects of the horizontal structure of the vortices, as a first step. The effects of the vertical structure of vortices (e.g., scattering into higher vertical modes; Dunphy and Lamb 2014) will be the next step. The initial vortices were in the gradient wind balance, which includes the geostrophic and cyclostrophic balances at both limits. Only cyclonic vortices were examined for stability because strong anticyclonic vortices are unstable for centripetal instability. The shape of the initial vortices was of the Rankine type:

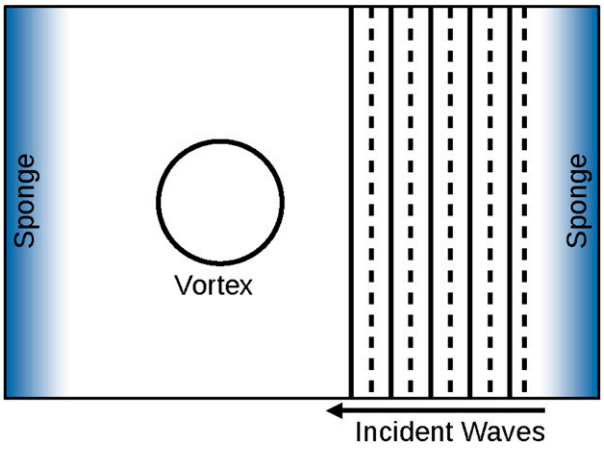

FIG. 1. Schematic of initial state in horizontal view. The circle represents an initial vortex. The vertical lines represent incident waves with ridges (solid) and troughs (dash).

$$V(r) = \begin{cases} V_0 \dfrac{r}{R} & (r < R) \\ V_0 \dfrac{R}{r} & (R \le r) \end{cases}, \tag{1}$$

and the Gaussian type:

$$V(r) = \frac{V_0 r}{\exp^{-1/2} R} \exp\left[- \left(\frac{r}{\sqrt{2} R} \right)^2 \right], \tag{2}$$

where V is the vortex flow speed, r is the radial distance from the center of the vortex, V_0 is the maximum flow speed of the vortex, and R is the radius at which the vortex flow speed is at the maximum. The Gaussian vortex is slightly reformulated to meet the definition of R.

The incident waves were monochromatic and had relatively small amplitudes and the vertical-mode structure $\eta = \eta_0 \sin(kx - \omega t)\sin(mz)$, where η is the vertical displacement, η_0 is the amplitude, k is the horizontal wavenumber, and m is the vertical wavenumber. The incident wave frequency ω is determined from the dispersion relation. The velocity components (u, v, w) were given as the solution of linear internal waves propagating toward the vortex. The velocity amplitude v_0 was set to be small ($v_0/c < 0.2$ in all experiments). Near-inertial waves and strongly nonhydrostatic waves were not considered.

The nondimensional parameter δ varied over a wide range (δ = [0.001, 1.7]) independent of kR, R_o, F_r, γ ($=f/\omega$), as shown in Fig. 2. The ranges of these nondimensional parameters were kR = [0.13, 30.0], R_o = [0.04, 2.0], F_r = [0.03, 1.5], γ = [0.02, 0.6]. In addition, ω/N = [0.008, 0.2], and the range $f \sim N$ was not considered. To change the nondimensional parameters, the dimensional parameters V_0, R, k, m, N were

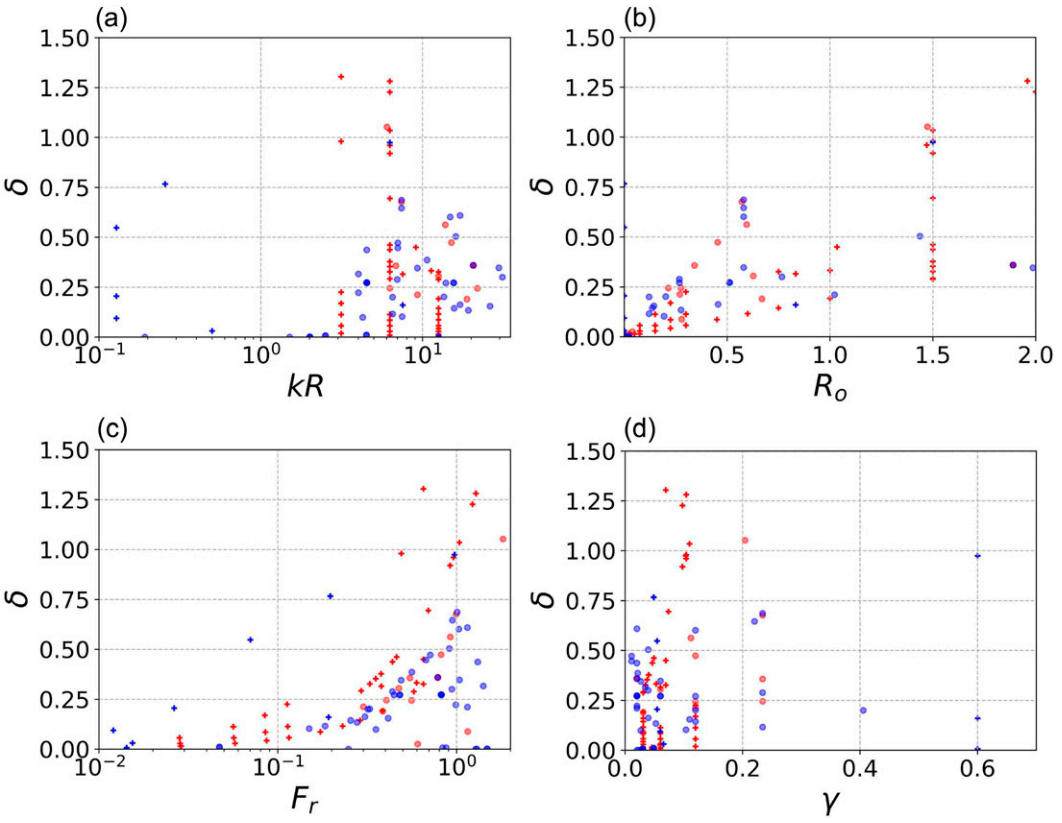

FIG. 2. Nondimensional parameters of the experiments; δ vs (a) kR, (b) R_o, (c) F_r, and (d) $\gamma = (f/\omega)$, where + and o symbols denote Rankine and Gaussian vortices, respectively. Red color indicates experiments for which the energy trapping rate and increase rate of vertical wavenumber were calculated (see section 4).

changed. It should be emphasized that δ can be changed independently of other nondimensional parameters, such as large (small) δ with small (large) kR, R_o, and F_r.

2) SETTINGS OF NUMERICAL MODEL

We used a nonhydrostatic, fully nonlinear three-dimensional model (but with the Boussinesq approximation) called "kinaco" (Matsumura and Hasumi 2008). We used an advection scheme of the fourth-order central difference, and viscosity and diffusion were implemented as Smagorinsky parameterization. The horizontal resolution was set at the finer of the following two: 1) resolving a vortex diameter with 50 grids or 2) resolving an incident wavelength with 100 grids. The vertical resolution was set at 100–200 grids per incident vertical wavelength. The model region was a rectangle with a constant depth. All horizontal boundaries were cyclic, but sponges were set on the right and left boundaries to avoid multiple interactions (Fig. 1). Free surface and slip-bottom conditions were adopted. The Coriolis parameter and buoyancy frequency were set to be uniform.

3) TRAPPED WAVE ENERGY AND VERTICAL WAVENUMBER

The dependence of the trapping rate of wave energy and increase rate of the vertical wavenumber (dm/dt) on δ is presented in section 4c. These rates were calculated as follows.

The trapping rate was defined as the ratio of the wave energy trapped in the vortex to the incident wave energy. The trapped energy was calculated as the difference between the incident wave energy and the wave energy outside the vortex after the passage of the incident waves. The wave energy was calculated as $E = (u^2 + v^2 + w^2)/2 + \int g\rho z dz$. The vortex periphery was defined as a flow speed of 5% of the maximum value. Accordingly, if wave breaking occurred in the vortex, its energy was counted as the trapped energy.

To estimate dm/dt, the vertical wavenumber was estimated in the vortex ($r < 2R$) as the number of zero crossings (minus one) in the vertical profile of the horizontally averaged vertical velocity. This roughly corresponds to the energy-containing wavenumber. The duration dt ranged from the start to the time when the shortest vertical wavelength became two vertical grid sizes, $2dz$, or to the time when transmitted waves reached the opposite boundary if the vertical wavenumber did not reach $2dz$.

c. *Estimation of δ in the Pacific Ocean*

To estimate values of δ that can be realized in the oceans, we estimated the four parameters R, V_0, k, and c for vortices and waves using the dataset of an ocean general circulation model (OGCM). Parameter δ indicates the strength of the interaction and the possibility of mixing, although δ is not

sufficient to determine the mixing strength, which also requires the incident wave energy.

The vortex parameters were estimated from the 1/30° version of the OGCM for the Earth Simulator (hereafter OFES30; Sasaki and Klein 2012), which permits submesoscale vortices. OFES30 has the finest grid size among those available. We used OFES30 even though tides were not included, because the resolution of the satellite altimetry, such as AVISO data (1/4°), would result in an underestimation of δ.

We detected closed streamline vortices by calculating the Okubo–Weiss parameter (OW) (Okubo 1970; Weiss 1991) from the surface flow velocity, after which we estimated R and V_0. An area was considered to be a vortex if OW < 0 in four or more adjacent grids. The former condition (OW < 0) extracts an area corresponding to a vortex core, where the azimuthal velocity is approximately given by $(V_0/R)r$. The purpose of the latter condition was to exclude noise. Radius R was calculated as the radius of an equivalent circular vortex with the same area, and V_0 was the maximum horizontal flow speed in the detected vortex.

To set the internal wave parameters k and c, we focused on the first vertical-mode waves with the M_2 tidal frequency. The range of γ in the experiments covered the M_2 frequency in the Pacific. The buoyancy frequency and Coriolis parameter were calculated at each vortex position using OFES30. Subsequently, k and c were calculated using the linear dispersion relation.

The magnitude of δ was assumed to be uniform for each vortex. The vortices with $\delta < 0.001$, which was the minimum δ in our experiments, were discarded because the lower limit of δ, above which nonnegligible scattering occurs, is uncertain. The use of OW and the threshold $\delta < 0.001$ could underestimate the number of weak vortices in the scattering regime.

3. Scaling analysis

Scaling analysis was conducted to derive a nondimensional parameter δ that is effective for understanding the present problem of waves incident on a vortex (Fig. 1). The usefulness of this parameter is supported by the numerical experiments (section 4).

a. Nondimensionalization

The governing equations are simplified to shallow water equations for an inviscid and nondiffusive fluid on the f plane. Shallow water equations, which roughly represent the horizontal structure evolution of a baroclinic mode, are relevant because internal waves of one vertical mode are incident on a barotropic vortex in the experiments. The scaling focuses on the initial stage of interaction, i.e., before nonlinearity changes the vertical structure. The governing equations in cylindrical coordinates are

$$\frac{\partial v_r}{\partial t} + v_r\frac{\partial v_r}{\partial r} + \frac{v_\theta}{r}\frac{\partial v_r}{\partial \theta} - \frac{v_\theta^2}{r} - fv_\theta = -g'\frac{\partial h}{\partial r}, \tag{3}$$

$$\frac{\partial v_\theta}{\partial t} + v_r\frac{\partial v_\theta}{\partial r} + \frac{v_\theta}{r}\frac{\partial v_\theta}{\partial \theta} + \frac{v_r v_\theta}{r} + fv_r = -\frac{g'}{r}\frac{\partial h}{\partial \theta}, \tag{4}$$

$$\frac{\partial h}{\partial t} + \frac{1}{r}\frac{\partial (rv_r h)}{\partial r} + \frac{1}{r}\frac{\partial (v_\theta h)}{\partial \theta} = 0, \tag{5}$$

where (r, θ) and (v_r, v_θ) are the radial and azimuthal coordinates and velocity, respectively, h is the layer thickness, and g' is the reduced gravity.

The most important aspect of our scaling is the use of different spatial and temporal scales for the vortices and waves. Such usage is based on the spatial scales of internal waves, possibly being much smaller, of the same order, or much larger than those of vortices in the oceans, as argued in the introduction.

To separate the scales, we first decompose the variables into a dynamically balanced vortex and deviation from it (disturbance part):

$$v_r(r, \theta, t) = v_r'(r, \theta, t), \tag{6}$$

$$v_\theta(r, \theta, t) = v_\theta'(r, \theta, t) + V(r), \tag{7}$$

$$h(r, \theta, t) = h'(r, \theta, t) + H(r) + \bar{H}, \tag{8}$$

where uppercase letters denote the vortex, lowercase letters with a prime denote the disturbance, and $\bar{H}$ is the mean layer thickness. Before waves encounter a vortex, the disturbance consists only of incident waves. After the encounter, the disturbance includes transmitted and scattered waves and other disturbances produced by wave–vortex interaction. We scale such disturbances with incident wave scales, considering that incident waves dominate the disturbance, at least at the initial stage of the interaction.

Second, to focus on the wave response in the vortex core, the governing equations [Eqs. (3)–(5)] are scaled with

$$t = \frac{1}{\omega}\tilde{t},\ \ r = \frac{1}{k}\tilde{r},\ \ (v_r',\ \ v_\theta') \sim v_0(v_r',\ \ v_\theta'),\ \ h' \sim h_0\tilde{h}',$$
$$V = \frac{V_0}{R}r = \frac{V_0}{Rk}\tilde{r},\ \ H = H_0\tilde{H}, \tag{9}$$

where the tilde denotes the nondimensional variables, and H is scaled by H_0. The variables of the coordinates are nondimensionalized by wave scales, whereas the vortex length scale is incorporated through the flow structure of a vortex core of the Rankine type [Eq. (1)]. The nondimensional equations become

$$\frac{\partial \tilde{v}_r'}{\partial \tilde{t}} + \left(\frac{1}{\omega}\frac{V_0}{R}\right)\left(\frac{\tilde{V}}{\tilde{r}}\frac{\partial \tilde{v}_r'}{\partial \theta} - 2\frac{\tilde{v}_\theta'\tilde{V}}{\tilde{r}} + \tilde{v}_r'\frac{\partial \tilde{V}}{\partial \tilde{r}}\right)$$
$$+ \left(\frac{v_0}{\omega/k}\right)\left(\tilde{v}_r'\frac{\partial \tilde{v}_r'}{\partial \tilde{r}} + \frac{\tilde{v}_\theta'}{\tilde{r}}\frac{\partial \tilde{v}_r'}{\partial \theta} - \frac{\tilde{v}_\theta'^2}{\tilde{r}}\right) - \left(\frac{f}{\omega}\right)\tilde{v}_\theta'$$
$$= -\left(\frac{g'h_0}{\omega/k}\frac{1}{v_0}\right)\frac{\partial \tilde{h}'}{\partial \tilde{r}}, \tag{10}$$

$$\frac{\partial \tilde{v}_\theta'}{\partial \tilde{t}} + \left(\frac{V_0}{R}\frac{1}{\omega}\right)\left(\tilde{v}_r'\frac{\partial \tilde{V}}{\partial r} + \frac{\tilde{v}_r'\tilde{V}}{\tilde{r}} + \frac{\tilde{V}}{\tilde{r}}\frac{\partial \tilde{v}_\theta'}{\partial \theta}\right)$$
$$+ \left(\frac{v_0}{\omega/k}\right)\left(\tilde{v}_r'\frac{\partial \tilde{v}_\theta'}{\partial \tilde{r}} + \frac{\tilde{v}_\theta'}{\tilde{r}}\frac{\partial \tilde{v}_\theta'}{\partial \theta} + \frac{\tilde{v}_\theta'\tilde{v}_r'}{\tilde{r}}\right) + \left(\frac{f}{\omega}\right)\tilde{v}_r'$$
$$= -\left(\frac{g'h_0}{\omega/k}\frac{1}{v_0}\right)\frac{1}{\tilde{r}}\frac{\partial \tilde{h}'}{\partial \tilde{r}}, \tag{11}$$

$$\frac{\partial \tilde{h}'}{\partial \tilde{t}} + \underbrace{\left(\frac{v_0}{\omega/k}\right)\left(\frac{\bar{H}}{h_0}\right)\left[\frac{1}{\tilde{r}}\left(\frac{\partial \tilde{r}\tilde{v}'_r}{\partial \tilde{r}} + \frac{\partial \tilde{v}'_\theta}{\partial \theta}\right)\right]}_{\text{(a)}} + \left(\frac{1}{\omega}\frac{V_0}{R}\right)\frac{\tilde{V}}{\tilde{r}}\frac{\partial \tilde{h}'}{\partial \theta}$$
$$+ \underbrace{\left(\frac{v_0}{\omega/k}\right)\left(\frac{H_0}{h_0}\right)\left[\frac{\tilde{H}}{\tilde{r}}\left(\frac{\partial \tilde{r}\tilde{v}'_r}{\partial \tilde{r}} + \frac{\partial \tilde{v}'_\theta}{\partial \theta}\right) + \tilde{v}'_r\frac{\partial \tilde{H}}{\partial \tilde{r}}\right]}_{\text{(b)}}$$
$$+ \underbrace{\left(\frac{v_0}{\omega/k}\right)\left[\frac{\tilde{h}'}{\tilde{r}}\left(\frac{\partial \tilde{r}\tilde{v}'_r}{\partial \tilde{r}} + \frac{\partial \tilde{v}'_\theta}{\partial \theta}\right) + \tilde{v}'_r\frac{\partial \tilde{h}'}{\partial \tilde{r}} + \frac{\tilde{v}'_\theta}{\tilde{r}}\frac{\partial \tilde{h}'}{\partial \theta}\right]}_{\text{(c)}} = 0. \tag{12}$$

Here, the dynamically balanced vortex part is subtracted.

Subsequently, we introduce simplifying assumptions and evaluate the terms in these equations. Considering linear internal waves, except near-inertial waves, we assume that the scales of the pressure gradient and temporal change terms are the same; i.e., $\partial v'_r/\partial t \approx -g'\partial h'/\partial r$. Then,

$$\omega v_0 \approx g' k h_0, \tag{13}$$

and thus the coefficient of the pressure gradient terms becomes unity. We assume that the wave Froude number is sufficiently small; i.e., small-amplitude internal waves, implying that the products of the wave variables can be ignored:

$$\frac{v_0}{\omega/k} = \frac{v_0}{c} \ll 1. \tag{14}$$

The coefficient of term a in Eq. (12), which represents convergence caused by wave velocity and the mean layer thickness, has the same scale as the temporal change term because

$$\left(\frac{v_0}{c}\right)\left(\frac{\bar{H}}{h_0}\right) \approx \frac{v_0}{c}\bar{H}\frac{g'k}{\omega v_0} = \frac{1}{c^2}g'\bar{H} \approx 1, \tag{15}$$

as in the case of the linear internal waves. The term c is negligible under the assumption of small-amplitude internal waves. The coefficient of term b is

$$\left(\frac{v_0}{\omega/k}\right)\left(\frac{H_0}{h_0}\right) = \frac{v_0}{c}\frac{H_0}{h_0}. \tag{16}$$

Accordingly, if $H_0/h_0 \lesssim 1$, which is satisfied by barotropic and relatively weak baroclinic vortices, we can ignore term b with at least the same degree of approximation, where we ignore the terms with the coefficient v_0/c, the wave Froude number. However, if $H_0/h_0 \gg 1$, which is satisfied by relatively strong baroclinic vortices, term b should be considered.

To evaluate term b for the latter case ($H_0/h_0 \gg 1$), we scale the displacement associated with a vortex $H = H_0\tilde{H}$, assuming that the vortex is in the gradient wind balance:

$$-\frac{V(r)^2}{r} - fV(r) = -g'\frac{\partial H(r)}{\partial r}. \tag{17}$$

This is nondimensionalized as using $g'\bar{H} = c^2 = \omega^2/k^2$,

$$\left(\frac{V_0}{Rk}\right)^2\tilde{r}^2 k\frac{1}{\tilde{r}} + f\frac{V_0}{Rk}\tilde{r} = k\frac{\omega^2}{k^2}\frac{H_0}{\bar{H}}\frac{\partial \tilde{H}}{\partial \tilde{r}}, \tag{18}$$

arranged as

$$\frac{\partial \tilde{H}}{\partial \tilde{r}} = \frac{\bar{H}}{H_0}(\delta^2 + \delta\gamma)\tilde{r}, \tag{19}$$

and integrated to yield

$$H = H_0\tilde{H} = \bar{H}\frac{\delta^2 + \delta\gamma}{2}\tilde{r}^2. \tag{20}$$

Therefore, the scale of term b is

$$\frac{v_0}{c}\frac{H_0}{h_0} \sim \frac{v_0}{c}\frac{\bar{H}}{h_0}\frac{\delta^2 + \delta\gamma}{2} \approx \delta\left(\frac{\delta + \gamma}{2}\right), \tag{21}$$

using Eq. (15). In the case of strong baroclinic vortices, both the advection of the displacement associated with the vortices by the wave velocity and the convergence caused by the displacement associated with the vortices and wave velocity must be included at a scale of $\delta(\delta + \gamma)/2$. However, the coefficient is negligible in the case of barotropic vortices, because the displacement associated with the vortices is small.

The scaled equations are summarized as follows, omitting the tilde:

$$\frac{\partial v_r}{\partial t} + \delta\left(\frac{V}{r}\frac{\partial v_r}{\partial \theta} - \frac{2Vv_\theta}{r} + v_r\frac{\partial V}{\partial r}\right) - \gamma v_\theta = -\frac{\partial h}{\partial r}, \tag{22}$$

$$\frac{\partial v_\theta}{\partial t} + \delta\left(\frac{V}{r}\frac{\partial v_\theta}{\partial \theta} + v_r\frac{dV}{dr} + v_r\frac{V}{r}\right) + \gamma v_r = -\frac{1}{r}\frac{\partial h}{\partial \theta}, \tag{23}$$

$$\frac{\partial h}{\partial t} + \left(\frac{1}{r}\frac{\partial r v_r}{\partial r} + \frac{1}{r}\frac{\partial v_\theta}{\partial \theta}\right) + \delta\frac{V}{r}\frac{\partial h}{\partial \theta} + \delta\left(\frac{\delta + \gamma}{2}\right)\left(\frac{H}{r}\frac{\partial r v_r}{\partial r} + \frac{H}{r}\frac{\partial v_\theta}{\partial \theta} + v_r\frac{\partial H}{\partial r}\right) = 0. \tag{24}$$

If $\delta \to 0$, these become the governing equations of the linear internal waves. The parameter δ appears in the coefficients of all terms introduced by the effects of the vortices.

b. Nondimensional parameters

The nondimensional parameter δ characterizes the wave response to a vortex core. The larger the δ, the stronger the wave response, because δ appears in the interaction terms. The case $\delta = 0$ represents free waves with no vortices. When $\delta \ll 1$, the wave response is linear or weakly nonlinear with a large, weak vortex relative to the incident waves. When $\delta \gtrsim 1$, a stronger wave response is expected, with a relatively small, strong vortex. The two former cases have been explored extensively; however, the latter case has not been investigated.

The parameter δ can be interpreted as the duration of the interaction. This is the ratio of the vortex turnover time V_0/R and wave period $1/(kc)$. This can be further transformed to $\delta = (V_0/c)(c/R)[1/(kc)]$; that is, the product of F_r ($=V_0/c$), a

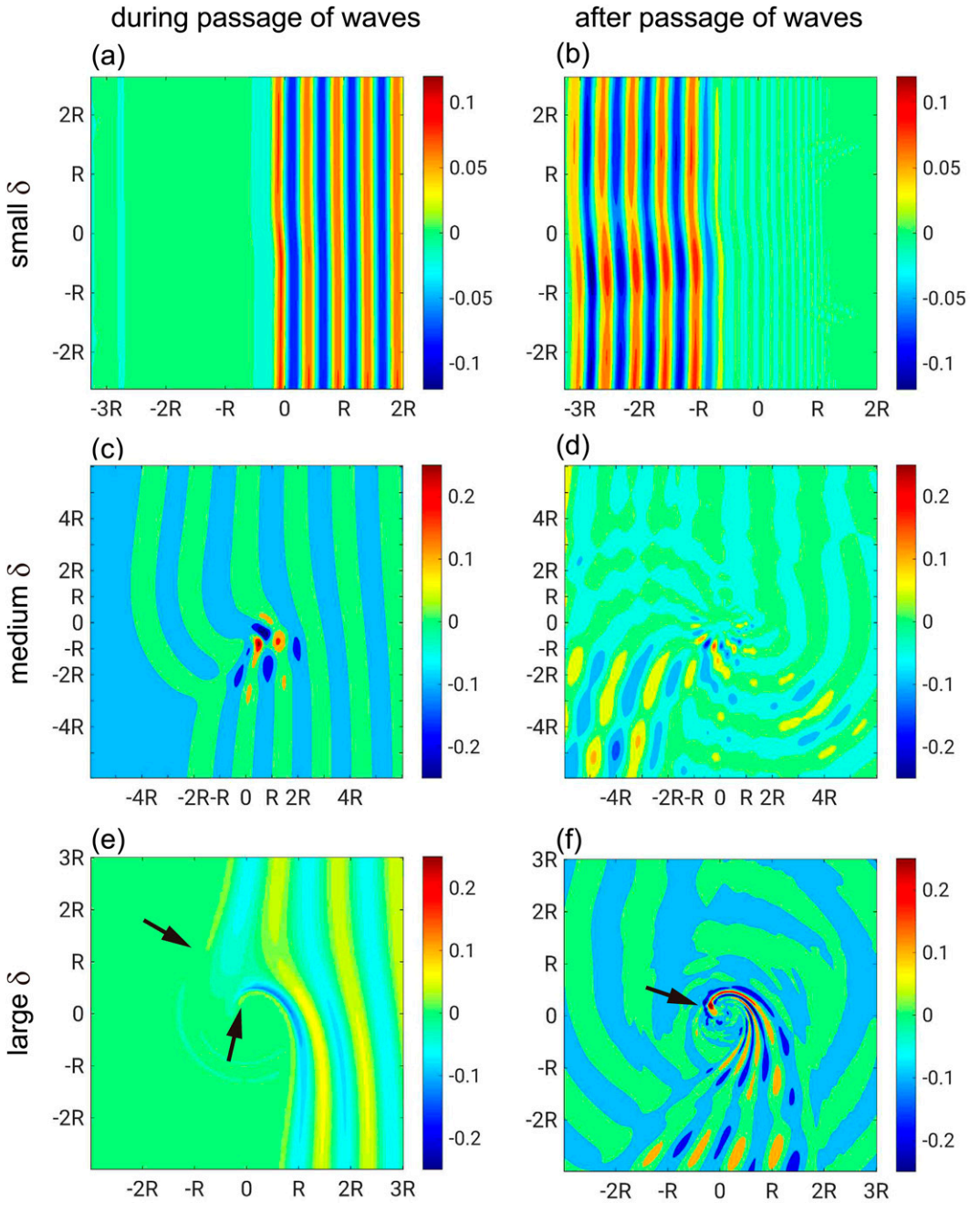

FIG. 3. Wave response for (a),(b) $\delta = 0.01$, (c),(d) $\delta = 0.16$, and (e),(f) $\delta = 0.72$, (left) during and (right) after passage of an incident wave through the vortex. The horizontal distribution of density anomaly (σ_θ) at the depth of an antinode of vertical velocity. The horizontal axes are scaled by vortex radius, R, with the vortex center at the origin. Arrows point to split waves in (e) and a focal point in (f).

measure of vortex strength, c/R, the inverse of the time it takes for waves to cross the vortex, and $1/(kc)$, the wave period. This implies that the strength of the wave response δ is represented as the relative strength of the vortex flow (F_r) divided by the nondimensional time during which waves are affected.

The parameter δ is related to R_o and F_r, which can be derived from the same shallow water equations but with different scaling, and are often used to scale wave–vortex interaction. Parameter δ $\{=[1/(kR)](V_0/c)\}$ becomes R_o $[=V_0/(fR)]$ when kc $(=\omega) \rightarrow f$; that is, the inertial period is selected for the time scale instead of the incident wave period. The parameter δ $\{=[1/(kR)](V_0/c)\}$ becomes F_r $(=V_0/c)$ when $kR \rightarrow 1$; that is, the length scales of the waves and vortices are the same. Accordingly, scaling using the Rossby number or Froude number

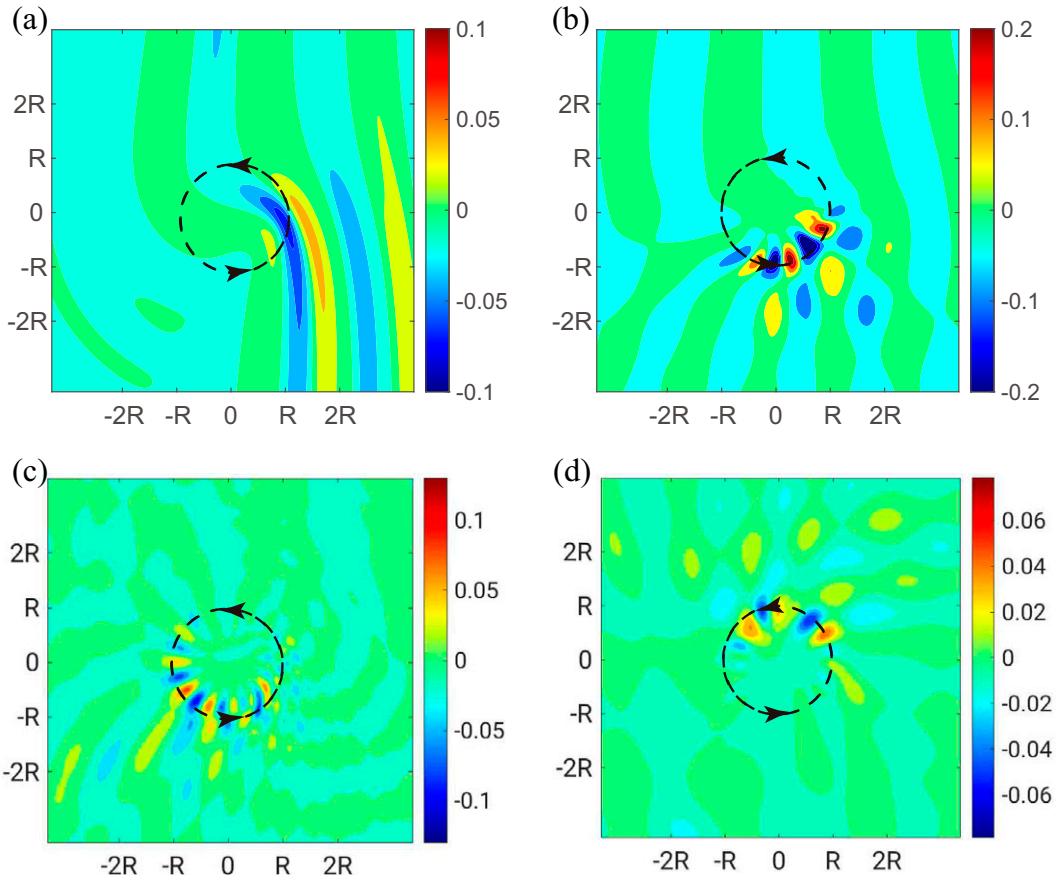

FIG. 4. Wheel-shaped trapped waves in the same experiment as Figs. 3c and 3d. (a) Bent and split incident waves, (b) generation of wheel-shaped trapped waves, (c) the first and (d) second laps of the circling trapped waves. The density anomaly is shown with the location and direction of the maximum vortex flow (dashed circle).

is a special case of scaling using δ. In particular, δ can be changed with R_o and/or F_r kept constant and vice versa. Therefore, δ is preferred here for scaling the interaction problem compared with R_o and F_r.

The case in which the dominant vertical mode is the same for both the waves and geostrophic vortices is noteworthy, although this is not the case in the present study. In this case, $L_d = c/f$, where L_d is the deformation radius. It follows that the time it takes for the wave to pass the vortex is $R/c \sim L_d/c = 1/f$ independent of the incident wave properties, although δ still depends on the wave properties through $\delta = (f/\omega)R_o \sim [1/(kR)]R_o$. In addition, attention is needed for near-inertial waves, particularly waves of zero horizontal wavenumber, for which $\delta \to \infty$.

4. Numerical experiments

The nondimensional parameter δ is expected to correspond to the strength of the interaction between the vortex and internal waves, and thus that of induced mixing. This section shows that the interaction is classified into three regimes, according to δ; the dependence on δ is then quantitatively explored to evaluate the transitions of these regimes.

a. Three regimes

As δ varies, the wave response changes qualitatively; that is, scattering for $\delta \leq 0.15$, the generation of trapped wheel-shaped waves for $0.15 < \delta \leq 0.4$, and trapped spiral-shaped waves for $\delta > 0.4$. Vortex response is also large in the last regime.

1) $\delta \leq 0.15$: SCATTERING REGIME

This parameter range is characterized by scattering and is hereafter referred to as the scattering regime. Figure 3 shows a plan view of the density disturbance; i.e., the vertical displacement by waves. The waves enter from the right-hand side and collide with a vortex placed at the center (Fig. 3a). All incident waves pass through the vortex, with some part refracted to form hot and cold spots (Fig. 3b), as reported by Dunphy and Lamb (2014). The vertical structure of the waves remains unchanged because the initial vortex is barotropic. The vortex also remains unchanged, as the waves are not broken or dissipated. This is consistent with the weak nonlinear theory.

2) $0.15 < \delta \leq 0.4$: WHEEL-TRAPPING REGIME

This parameter range is characterized by wheel-shaped trapped waves and backscattered waves and is hereafter

referred to as the wheel-trapping regime. In contrast to the scattering regime, the trapped waves cause vertical mixing.

Figures 3c and 3d show the characteristic features of the wheel-trapping regime. Although the main part of the incident waves passes through, the rest are trapped in the vortex and form wheel-shaped waves (Fig. 3d). The trapped waves remain in the vortex, even after the incident waves pass through. In addition, the propagation direction of the scattered waves is deflected more than in the scattering regime, causing backscattered waves.

Wheel-shaped waves are generated, as shown in Fig. 4. 1) Incident waves are strongly bent by the vortex and split into two near the maximum of the opposing flow (i.e., the flow against the incident waves; Fig. 4a). 2) The split wave on the opposing-flow side near the vortex flow maximum increases in both amplitude and horizontal wavenumber and propagates along the vortex flow maximum against the flow (Fig. 4b). It then forms a wheel-shaped wave (Fig. 4c), which continues to circle along the vortex core (Fig. 4d). In other words, the wheel-shaped wave is trapped in the vortex. 3) The rest of the incident waves pass through the vortex; that is, both the other part on the opposing-flow side sufficiently distant from the vortex core and the split waves on the following-flow side (Figs. 4b,c). The generation of wheel-shaped waves is always accompanied by a split of the incident waves, which does not occur in the scattering regime.

The properties of the wheel-shaped waves are as follows.

- The horizontal structure is characterized by isophase lines extending radially from the vortex center, with the amplitude maximum located near the location of the vortex flow maximum (R). The phase velocity is directed against vortex flow.
- The frequency is similar to that of the incident wave.
- The azimuthal wavenumber is approximately 8, corresponding to $1.69k$ at the vortex flow maximum in the experiment of Figs. 3c and 3d.
- In the radial direction, the number of amplitude peaks varies from one to four in the experiments, with a narrower peak width and smaller amplitude toward the outside.

These features suggest that wheel-shaped waves are different from the near-inertial vortex-trapped mode in anticyclones because the latter is characterized by a horizontally uniform phase and amplitude maximum at the vortex center (e.g., Kafiabad et al. 2021). In fact, wheel-shaped waves are superinertial, and the existence of wheel-shaped waves is associated with the gradient of the background vorticity associated with a vortex (details to be discussed in a following paper along with an analytical solution).

Vertical mixing occurs in this regime through two processes. 1) Some of the split waves break and cause vertical mixing because of the increase in the horizontal wavenumber by nonlinear interaction when wheel-shaped waves are generated. 2) The wheel-shaped waves eventually dissipate and cause mixing in the vortex in which the waves are trapped, although wave breaking does not occur immediately. The dissipation of wave energy and associated release of pseudomomentum should modify the vortex. From this perspective, the interaction is not catalytic in the wheel-trapping regime.

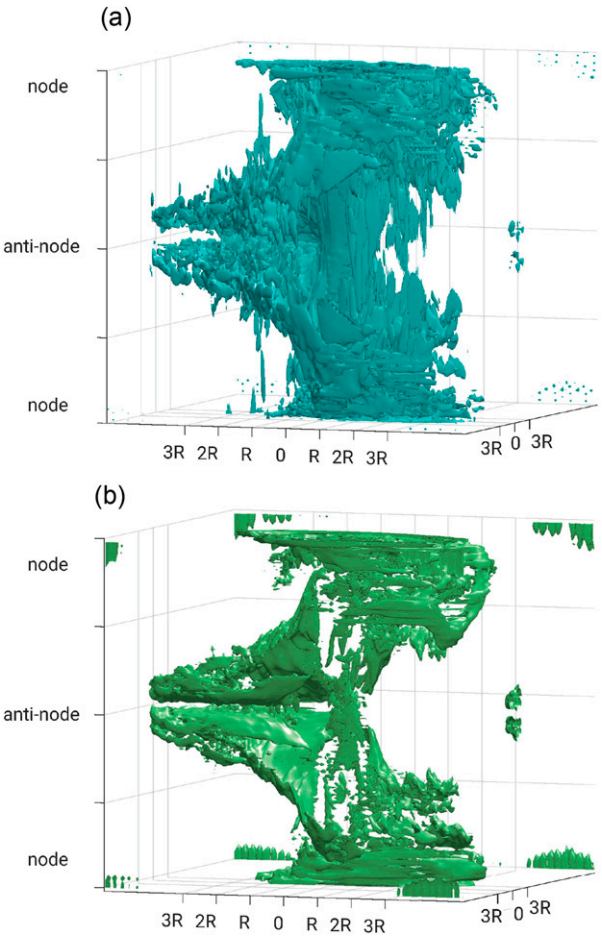

FIG. 5. (a) Three-dimensional view of the vortex deformed by incident waves in the spiral-trapping regime in the experiment of Figs. 3e and 3f. Isosurface of vertical vorticity 0.0003 (s^{-1}) is plotted after 8 incident-wave periods since the incident wave reaches $x = R$ (the vortex core). (b) As in (a), but for vertical shear of 0.02 (s^{-1}).

3) $\delta > 0.4$: SPIRAL-TRAPPING REGIME

This parameter range is characterized by trapped spiral-shaped waves and is hereafter referred to as the spiral-trapping regime. Most of the waves incident on the vortex are trapped, forming a spiral shape (Figs. 3e,f) and causing more vigorous vertical mixing compared with the wheel-trapping regime.

Spiral-shaped waves are generated as follows. 1) Incident waves on the opposing-flow side are bent so strongly that some of the wave rays are advected to the following flow side (Fig. 3e). 2) The advected wave rays form a focal point (arrow in Fig. 3f), around which the focusing and shrinking of the wavelength increase the wave amplitude. 3) Wavefronts are strongly bent near the focal point and split into those on the vortex core side and those on the other side (arrows in Fig. 3e). 4) The split waves on the core side move with both the phase velocity

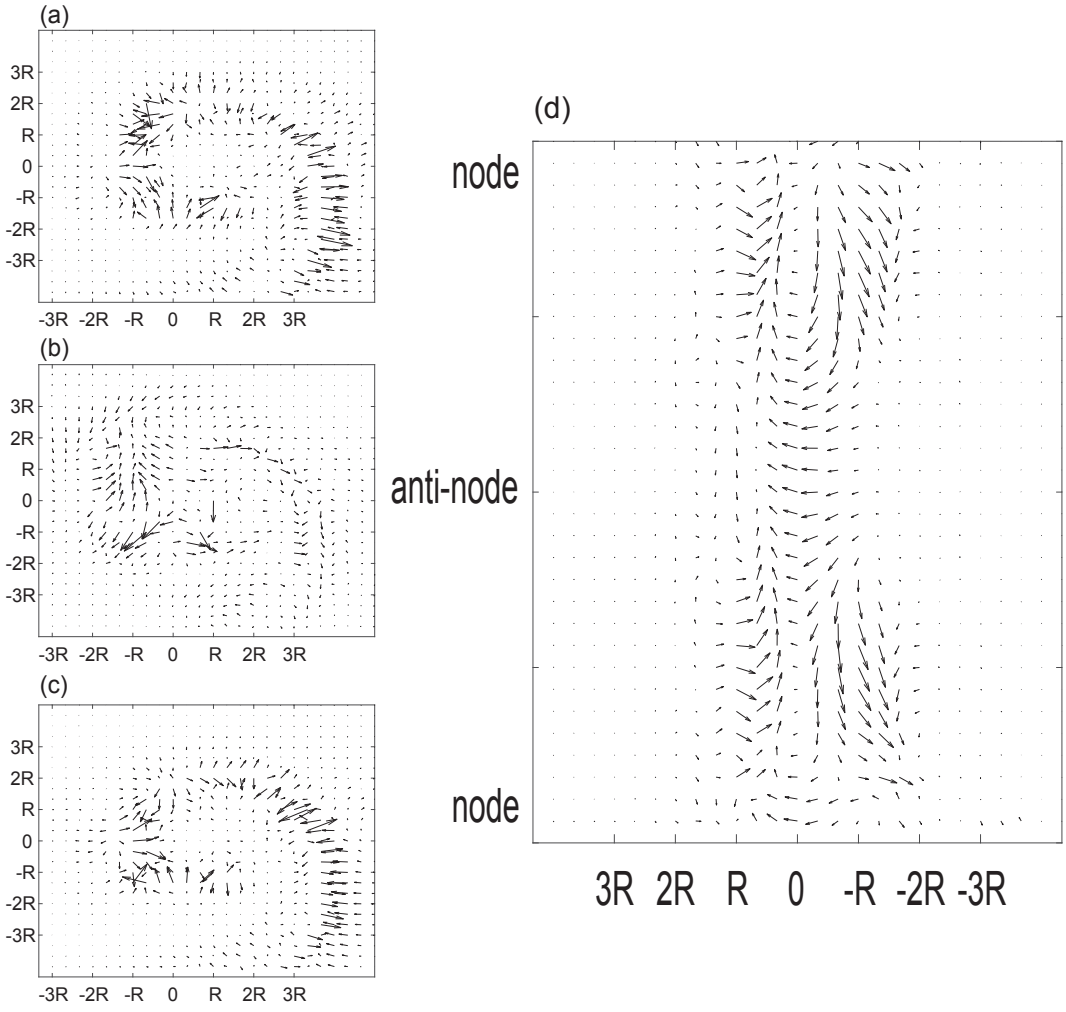

FIG. 6. The horizontal divergence of pseudomomentum flux at the (a) upper (node), (b) middle (antinode), and (c) lower (node) levels of the vortex in the experiment of Figs. 3e and 3f. Values are temporally averaged from 6 to 8 incident wave periods. The horizontal axes are scaled by vortex radius, R. (d) As in (a)–(c), but for the y–z section, averaged in the x direction from $-2R$ to $2R$.

directed to the center and advection by the vortex flow, and therefore, form a spiral shape. Split waves on the other side pass through the vortex.

The properties of the spiral-shaped waves are as follows:

- The horizontal structure is characterized by isophase lines that spiral from the periphery of the vortex core (Figs. 3e,f).
- The phase velocity is directed toward the vortex center.
- The frequency is approximately equal to that of the incident waves.
- The radial wavenumber increases as the spiral-shaped waves moves closer to the vortex center.

The breaking of incident waves occurs in this spiral-trapping regime, as wave energy is concentrated horizontally through three processes. 1) The spiral propagation of spiral-shaped waves increases the horizontal wavenumber and causes wave breaking in most cases. After breaking, wheel-shaped waves can be generated in certain cases. Near the transition of the regimes, spiral-shaped waves do not break and a focal point does not form, although wave rays are concentrated at a point, the location of which shifts against the vortex flow with decreasing δ. 2) When δ is sufficiently large, a critical layer is formed near the vortex flow maximum on the side where the incident waves enter, leading to wave breaking. 3) When the amplitude of the incident waves is sufficiently large, the concentration of the waves at the focal point results in wave breaking.

4) VORTEX DEFORMATION AND VERTICAL MIXING IN THE SPIRAL-TRAPPING REGIME

The vortex structure is changed by wave breaking, further enhancing vertical mixing. The vortex shape becomes zigzag in the vertical direction after wave breaking (Fig. 5). The vortex moves horizontally to the following (opposing)-flow side

around the heights of the antinode (node) for the vertical velocity of the incident waves. The number of zigzag bends is determined by the vertical mode number of the incident waves. The zigzag amplitude depends on the incident wave amplitude and the strength of stratification.

The above vortex deformation is caused by the mean flow generated by the release of wave pseudomomentum caused by wave breaking (for pseudomomentum, please refer to Bühler 2014). The divergence of the pseudomomentum flux (Liu et al. 2019) was calculated for each direction and is shown as a vector in Fig. 6. Around the middepth (the antinode of the first-mode incident waves), divergence is caused mainly by wave breaking near the focal point and is directed to the following-flow side (Fig. 6b). At lower and upper depths (the nodes of the first-mode incident waves), divergence is caused by the horizontal shrinking of the spiral-shaped waves, leading to wave breaking, and is directed to the opposite-flow side (Figs. 6a,c).

Figure 6d shows the y–z distribution of the divergence averaged in the x direction in the range where the vortex is significantly deformed. By averaging, the consistency becomes clearer between the y component of the divergence (Fig. 6d) and the vortex deformation (Fig. 5a). The vertical component is produced by breaking of relatively large-amplitude incident waves. The mean flow accelerates up to 0.15 m s^{-1} due to large wave momentum associated with large amplitude, causing large vortex deformation.

The vortex deformation induces strong vertical shear (Figs. 5a,b), which in turn increases the vertical wavenumber of the incident and trapped waves and causes vertical mixing. Figure 7 shows the temporal evolution of the vertical wavenumber of the energy-containing waves in the vortex [section 2b(3)]. Initially, the vertical wavenumber gradually increases because of wave breaking caused by an increase in the horizontal wavenumber. After the vortex deforms significantly (1.5 incident wave periods), the vertical wavenumber increases exponentially. Finally, it becomes saturated as it increases sufficiently to cause wave breaking. The exponential increase in the vertical wavenumber is caused by the vertical shear associated with the vortex deformation. Our results (black line in Fig. 7) match the prediction of the wave capture theory (red line, Bühler and McIntyre 2005; Polzin 2008).

Therefore, in this regime, the vortex is not a catalyst. A vortex traps waves and causes breaking of the incident and trapped waves. Wave-breaking deforms the vortex. The vertical shear of the deformed vortex enhances the vertical mixing. Such a strong interaction occurs between a vortex and waves in the spiral-trapping regime.

b. *Comparisons for kR and vortex shape*

Classification into the three regimes by δ holds true qualitatively for the parameter ranges shown in Fig. 2, even when parameters constructing δ vary but keeping δ or when a vortex is not of the Rankine type. Here, we compare cases of different kR (or F_r) values and Gaussian-type vortices.

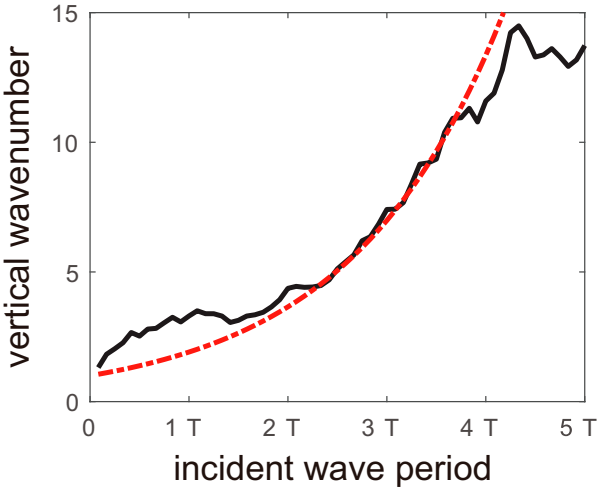

FIG. 7. Time evolution of vertical wavenumber in the vortex (black) and the prediction by wave capture theory (red) for the experiment of Figs. 3e and 3f.

Even when the length scale ratio of the vortex and incident waves kR changes, the regime is determined by δ. Figure 8 shows the typical wave responses for each regime. The cases of small and large kR with the same δ are aligned in rows and those with the same kR with different δ are aligned in the columns. The responses in each row for the same δ are similar. For a small δ (top row), incident waves are transmitted and scattered to form the contrast of the energy flux in both cases (left and middle columns). In all cases, both the shape of the scattered wave beam on the opposing-flow side and the phase shift between the opposing and following-flow sides are similar. For a medium δ (middle row), wheel-shaped waves form in all cases with slightly different structures. The contours of zero displacement extend approximately along the radial and azimuthal directions for large kR cases, but not for small kR cases. For a large δ (bottom row), spiral-shaped waves formed in all cases, although the position of a focal point differs depending on δ.

The same kR (or F_r) results in different responses when δ differs. The top, middle, and bottom rows of the left and middle columns are characterized by scattering, wheel-shaped waves, and spiral-shaped waves, respectively. The response is different (same) when δ is different (same) for the same (different) $F_r = V_0/c$ because $\delta = F_r/(kR)$. Therefore, F_r and R_o are not suitable for classifying wave–vortex interactions in the three regimes.

The Gaussian- and Rankine-type vortices cause similar responses, as shown in the right column of Fig. 8. Compared with Rankine-type vortices, the characteristic features form in the same manner: scattered waves and energy contrast ($\delta \leq 0.15$), wheel-shaped waves and side/backward scattering ($0.15 < \delta \leq 0.4$), and spiral-shaped waves and foci ($\delta > 0.4$). After wave breaking in the spiral-trapping regime, disturbances confined in a vortex are produced more frequently in Gaussian cases than in Rankine. These results suggest that the flow structure in a vortex core does not need to be strictly $(V_0/R)r$ in order to produce similar results.

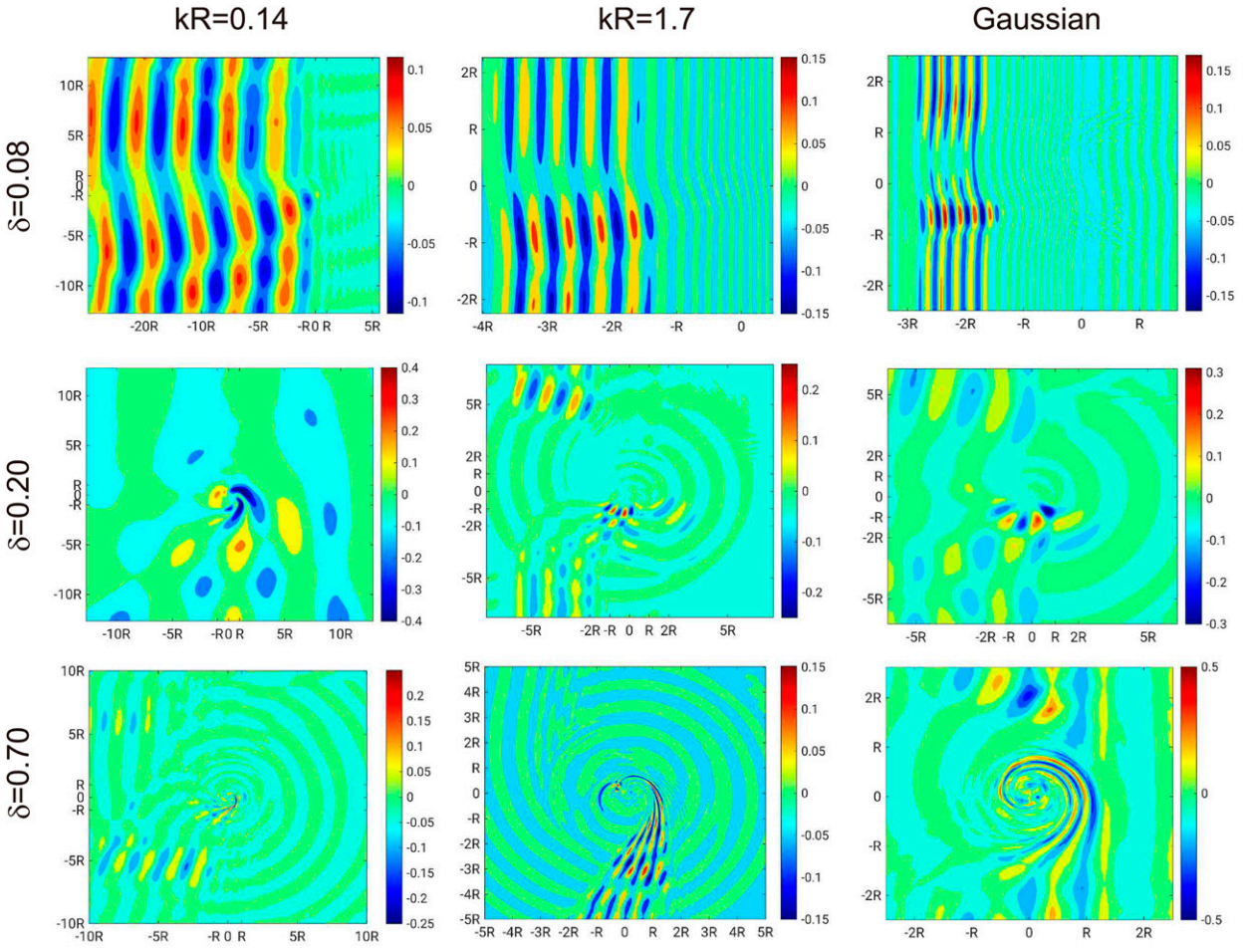

FIG. 8. Density anomaly after passage of incident waves but for (left) $kR = 0.14$, (center) $kR = 1.7$, and (right) Gaussian vortices in the (top) scattering $\delta = 0.08$, (middle) wheel-trapping $\delta = 0.20$, and (bottom) spiral-trapping regime $\delta = 0.70$.

c. *Classification of regimes by* δ

To classify the regimes by δ quantitatively, we use the trapping rate of the wave energy and the increase rate of vertical wavenumber (dm/dt) in a vortex against δ [section 2b(3)] shown in Figs. 9a and 10a, respectively. These are good measures because wave trapping occurs in the wheel- and spiral-trapping regimes, but not in the scattering regime, and because dm/dt depends on the degree of vortex deformation.

As expected, both the trapping rate and dm/dt depend strongly on δ, reflecting the three regimes. The trapping rate is almost zero for $\delta \leq 0.15$, whereas it increases with increasing δ for $0.15 < \delta$, corresponding to the formation of wheel- and spiral-shaped waves. The slope of the trapping rate against δ becomes gradual at approximately $\delta = 0.4$ for both Rankine and Gaussian vortices, suggesting the transition between the wheel and spiral-trapping regimes. The slope of dm/dt against δ also becomes gradual around $\delta = 0.4$, as the vortex deformation becomes sufficiently large. Interestingly, Gaussian vortices tend to show higher trapping rates and dm/dt than Rankine vortices, though we do not pursue this issue here.

Combining these two scatterplots, we selected the thresholds of δ to be 0.15 and 0.4, which are consistent with visual check. Nevertheless, these threshold values are rough estimates, and the values can change depending on the definitions or measurement methods. In fact, the transitions between regimes are gradual and continuous. In the transition from the scattering regime to the wheel-trapping regime, backscattered waves do not appear in some cases; therefore, the wheel-trapping regime is distinguished by the generation of wheel-shaped waves. In certain cases, both wheel- and spiral-shaped waves are generated; we regard such cases as the spiral-trapping regime.

The trapping rate and dm/dt against kR, R_o, and F_r scatter more than those against δ, although there are some correlations. Furthermore, the scatterplots against F_r have noticeable exceptions near the horizontal axes, and the scatterplots against R_o have surprisingly large scatter. These results suggest that δ is more useful for three-regime classification.

It is noteworthy that both the trapping rate and dm/dt increase monotonically with increasing δ, suggesting that δ is an index of the mixing potential. This is because an increase in the trapping rate indicates more dissipation in a vortex, and

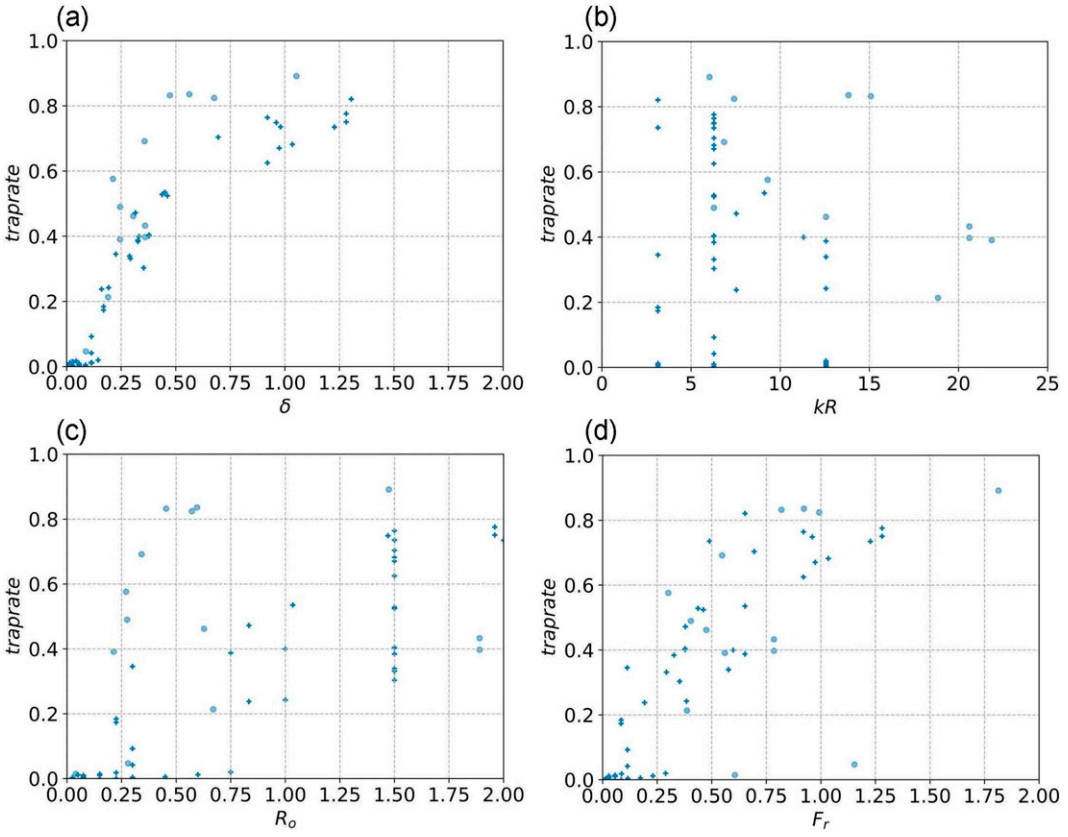

FIG. 9. Trapping rate of wave energy in a vortex vs nondimensional numbers: (a) δ, (b) kR, (c) R_o, and (d) F_r. Rankine and Gaussian cases are denoted by + and o symbols, respectively.

an increase in vertical wavenumbers is favorable for wave breaking.

5. Distribution of δ in the Pacific using OGCM output

As discussed, δ is a good index of the response of incident waves and the potential for mixing. Here, δ is estimated in the Pacific Ocean using OFES30.

a. Annual mean distribution of δ

Figure 11 shows a map of the annual frequency of δ in the scattering, wheel-trapping, and spiral-trapping regimes. Both the scattering and wheel-trapping regimes are broadly found in the Pacific Ocean, specifically in regions of high eddy kinetic energy in the OGCM (Sasaki et al. 2017), and/or large-eddy amplitudes estimated from satellite altimetry (Chelton et al. 2011). In particular, high frequencies are distributed along the Kuroshio and Kuroshio Extension. In addition, the frequency is relatively high around straits or islands (e.g., the Indonesian Archipelago and Kuril Islands), near coastal areas (e.g., the Gulf of Alaska and southwestern South China Sea), along strong currents (e.g., the East Kast Kamchatka Current and the Alaskan Stream), an active eddy region extending from the Subtropical Countercurrent around 25°N to roughly east-southeast, and in the equatorial region. Vortices in the spiral-trapping regime are mostly concentrated in the Kuroshio, Kuroshio Extension, and Torres Strait regions.

The histogram of δ (Fig. 12a) indicates that many vortices exist in the trapping regimes (wheel- and spiral-trapping regimes). The frequency has one peak in the scattering regime and gradually decreases in the wheel- and spiral-trapping regimes. It should be emphasized that the median of δ is larger than the threshold between the scattering and wheel-trapping regimes ($\delta = 0.15$). The median slightly decreases if eddies with $\delta < 0.001$ are not discarded. Nevertheless, wheel- and spiral-trapping regimes have a substantial percentage of eddies.

Figure 12b shows the horizontal aspect ratio of the vortices against δ. Most vortices are nearly circular with an aspect ratio of less than two, particularly for vortices of large δ. This supports the use of circular vortices in our experiments.

b. Seasonal variation of δ

The distribution of δ varies with the season in terms of its extent and magnitude. Large δ (>0.15, wheel- and spiral-trapping regimes) are distributed more broadly in winter (Fig. 13). Even in the other seasons, a large δ is distributed in strong current regions. Seasonal variation in δ suggests heightened mixing potential in active eddy regions such as the Kuroshio and its extension in winter and the Indonesian Archipelago in fall. The

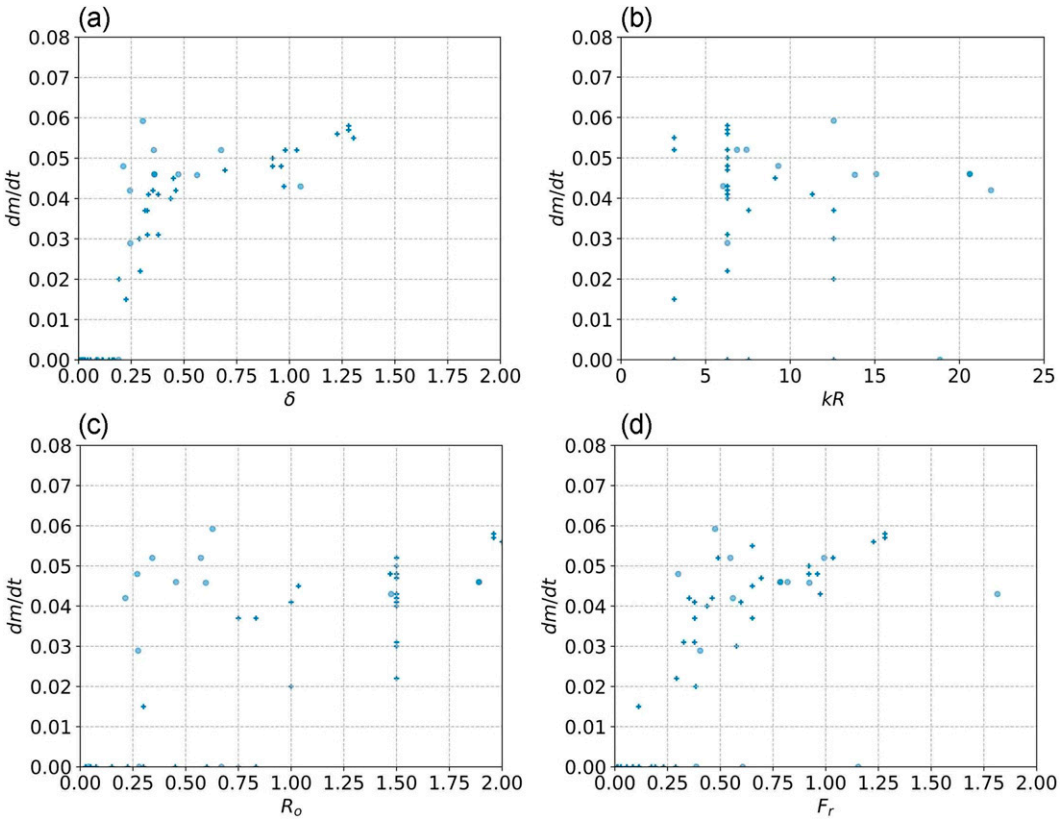

FIG. 10. As in Fig. 9, but for the increase rate of vertical wavenumber in a vortex.

former seasonal variation is consistent with the mixing strength estimated by Whalen et al. (2018), although their findings were attributed to wind variation.

The seasonal changes in δ and the eddy activity coincide. Figure 14 shows the monthly averaged median of δ, number of vortices, and median of vortex size. The median δ is large from December to February, and small from May to September. When the median δ increases, the number of vortices increases and the vortex size decreases. These changes are caused by active submesoscale eddies in winter (Sasaki et al. 2014) and seasonal variation around the Indonesian Archipelago. Although mesoscale eddies are dominant in summer and fall, wheel- and spiral-trapping regimes still occur. This implies that strong mesoscale eddies can trap the incident internal waves and induce mixing. It should be noted that the vortex size here is roughly 2 times smaller than the usual definition based on the deviation in sea surface height (Chelton et al. 2011) because of the vortex detection method used.

6. Summary and discussion

a. Summary of results

Although internal wave–vortex interactions affect vertical mixing, previous studies have focused on weak large vortices relative to waves, and the interactions with strong small vortices remain unexplored. Here, we investigated the interaction between a stable vortex and internal waves incident on the side in a broad parameter range ($\delta = [0.001, 1.7]$, $R_o = [0.04, 2.0]$, $F_r = [0.03, 1.5]$, $kR = [0.13, 30.0]$), except for near-inertial waves and found the following. 1) The internal wave–vortex interaction can be classified into three regimes by the nondimensional parameter δ: a regime of previously known scattering ($\delta \leq 0.15$), and the newly identified wheel-trapping ($0.15 < \delta \leq 0.4$) and spiral-trapping ($\delta > 0.4$) regimes. 2) Newly discovered wheel-shaped waves and backscattered waves occur in the wheel-trapping regime. In the spiral-trapping regime, 3) spiral-shaped waves and focal points form and 4) strong interaction through wave breaking and vortex deformation occurs. 5) All three regimes can occur in the Pacific Ocean with seasonal variation. Each of these findings are summarized below.

1) The nondimensional parameter δ, defined as $\delta = (V/R)[1/(kc)]$, appears in the coefficients of all terms introduced by the vortex effects in our scaled shallow-water equations, when the spatial and temporal scales of the vortex and waves are distinguished explicitly. The strength of possible mixing varies with the regime (i.e., δ), because both the trapping rate of the incident waves and the increase rate in the vertical wavenumber increase with increasing δ.
2) Wheel-shaped waves circle around the vortex core, with isophase lines extending radially from the vortex center and with the amplitude maximum aligned along the

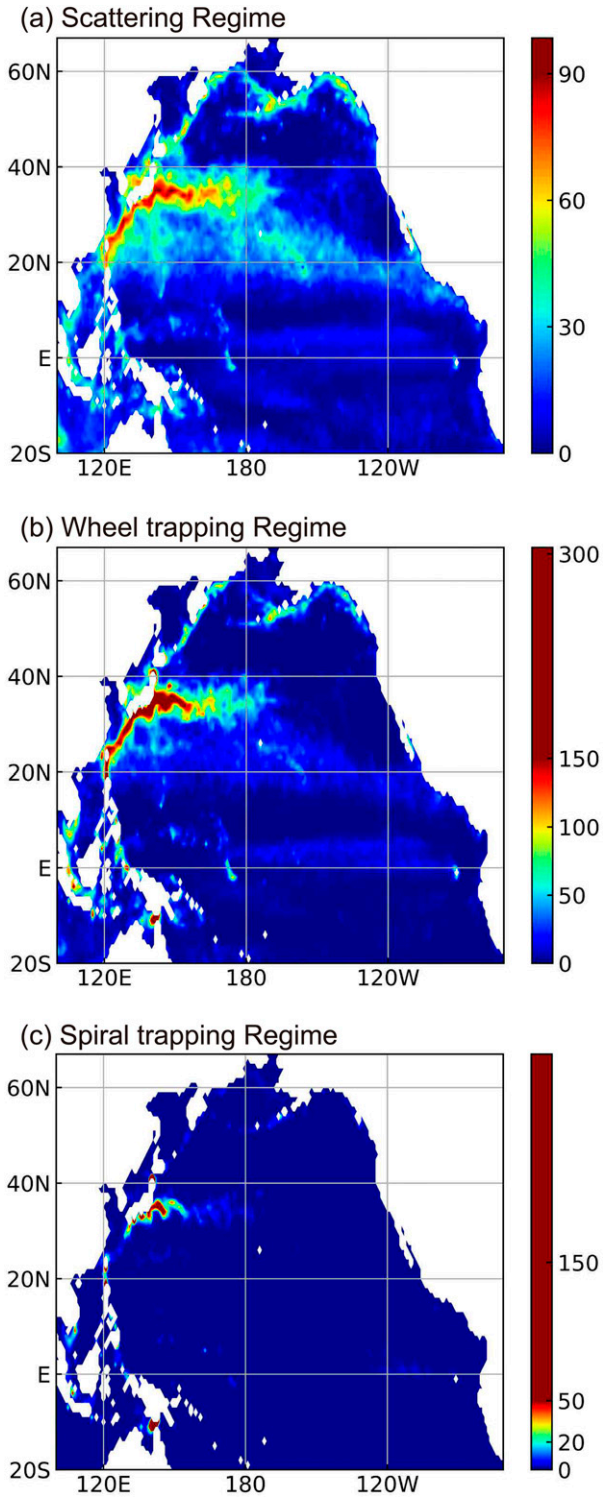

FIG. 11. Annual frequency of vortices in the (a) scattering, (b) wheel-trapping, and (c) spiral-trapping regimes estimated from the 1/30° version of the ocean general circulation model (OGCM) for the Earth Simulator (OFES30) in the Pacific Ocean in 2003 and plotted with $1^\circ \times 1^\circ$ bin.

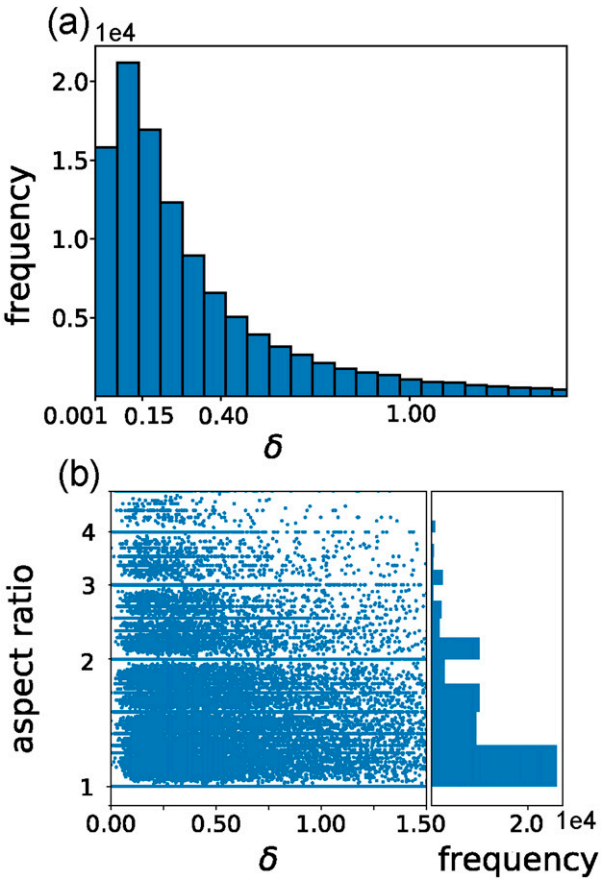

FIG. 12. (a) Histogram of δ in the Pacific Ocean. (b) Horizontal aspect ratio of eddies vs δ with histogram of the aspect ratio.

vortex flow maximum. Their frequency is almost equal to the incident wave frequency; hence, it is superinertial. Wheel-shaped waves eventually dissipate in the vortex, leading to mixing. Backscattered waves also form in this wheel-trapping regime.

Note that the wheel-shaped waves differ from the near-inertial vortex-trapped mode, which is attributed to a decrease in the effective inertial frequency in an anticyclone (Kunze and Boss 1998; Smith 1999). Furthermore, trapping of wheel-shaped (and spiral-shaped) waves in a cyclone shown in this study contrasts with the expulsion of near-inertial waves from a cyclone shown by Kafiabad et al. (2021). In fact, the latter expulsion would be caused by a higher effective inertial frequency in a cyclone. This is not the case for wheel-shaped waves.

3) The formation of both spiral-shaped waves and a focal point results in strong mixing. As the spiral shape develops, radial wavenumber increases, resulting in wave breaking. When δ is sufficiently large, the focal point is formed, around which both focusing and shrinking of the wavelength increase the wave amplitude, leading to wave breaking.

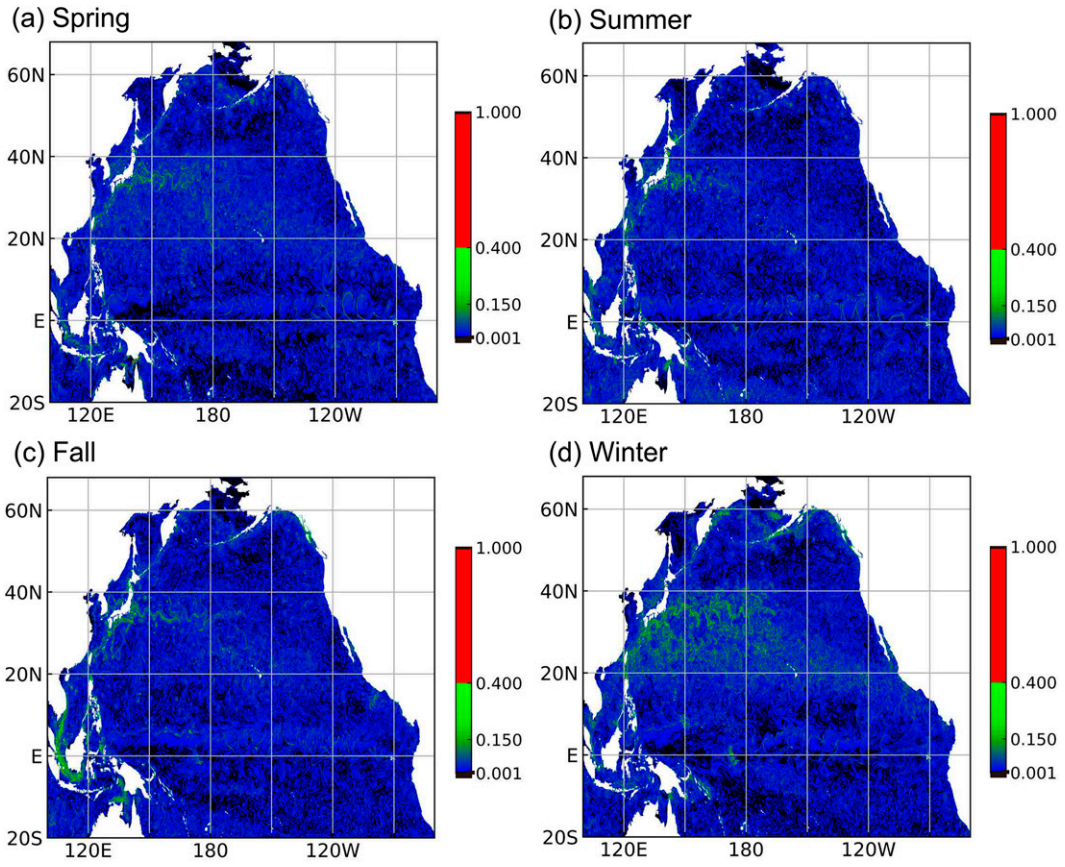

FIG. 13. Daily distributions of δ in (a) spring (8 Jan), (b) summer (13 Sep), (c) fall (21 Dec), and (d) winter (15 Mar) in 2003. Blue, green, and red represent the scattering, wheel-trapping, and spiral-trapping regimes, respectively. Black denotes $\delta < 0.001$, the minimum δ in our experiments. The resolution is 1/30° × 1/30°.

4) A vortex is deformed and interacts strongly with the incident waves in the spiral-trapping regime. As wave breaking releases wave pseudomomentum, the mean flow is produced in different directions at the wave nodes and antinodes, and deforms the vortex to a zigzag shape in the vertical direction. Vertical shear associated with a zigzag shape increases the vertical wavenumber and enhances mixing.
5) The estimated δ distribution in the Pacific Ocean shows that the mixing caused by the wheel- and spiral-trapping regimes can occur in active eddy regions. Distribution and magnitude of δ vary significantly from season to season. More vortices with large δ values (wheel- and spiral-trapping regimes) are distributed more broadly in winter. The seasonal variation in δ is associated largely with submesoscale eddy activity, although a significant proportion of mesoscale eddies have $\delta > 0.15$.

b. *Implications and limitations of results*

Our findings have implications for vertical mixing, its spatiotemporal variation, and theoretical interest. Wheel- and spiral-shaped waves, focal points, and deformed vortices in the wheel- and spiral-trapping regimes are new dynamical processes that lead to mixing. In fact, wave–vortex interaction has not been listed as a mixing mechanism in recent reviews (MacKinnon et al. 2017; Whalen 2021), although the importance of scattering in the wave properties has been highlighted. Thus, understanding of these processes would be needed for better estimates of the global distribution of vertical mixing.

It is of particular interest that the resulting mixing varies as the eddy field varies. Previous studies have usually neglected background flow when estimating mixing due to the internal waves generated by tides or geostrophic flow over topography (e.g., de Lavergne et al. 2020; Nikurashin and Ferrari 2011). However, strong and small vortices can cause mixing when they encounter internal waves. This implies that through variation in eddies, variation in the large-scale field can cause both spatial and temporal variations in mixing, including at seasonal, interannual, and longer time scales. For example, although the forcing of internal tides has small temporal variation, seasonal variation in the eddy field can change the mixing potential (or distribution), as discussed in section 5. Such seasonal variation in the interaction strength is consistent with the seasonal variation in diffusivity estimated by Whalen et al. (2018).

In addition, the interaction is expected to be stronger in the upper ocean, where eddies are abundant, in contrast to topographic scattering (e.g., Müller and Xu 1992; Nakamura and Awaji 2009).

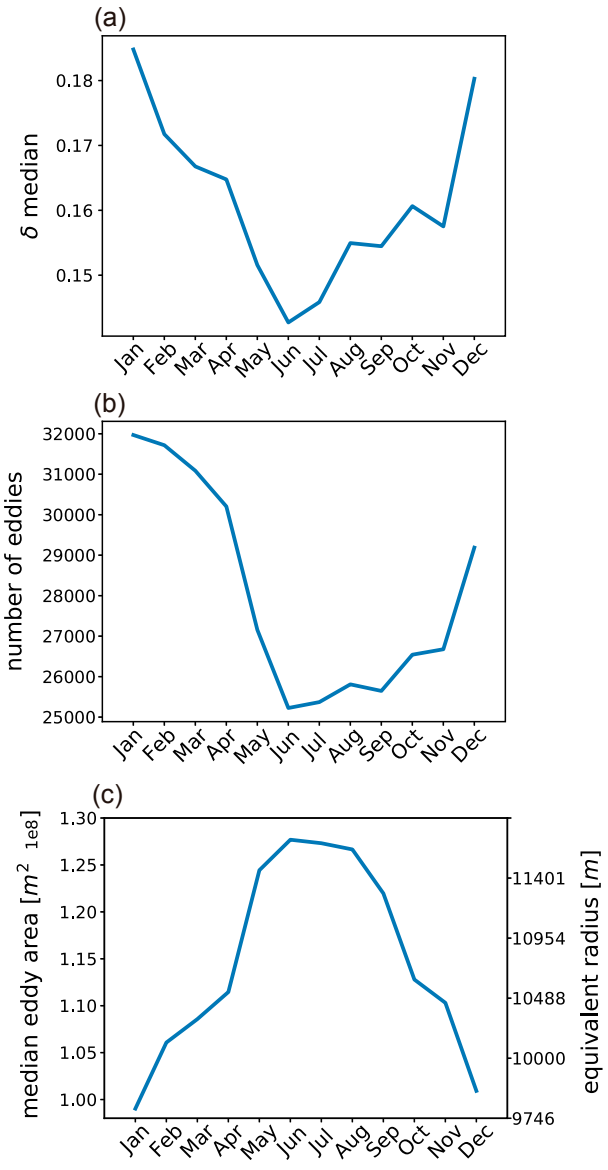

FIG. 14. Monthly averages of (a) median δ, (b) number of vortices, and (c) median vortex area (m^2) and equivalent radius (m) for left and right axes, respectively.

Thus, it could affect the ecosystem, air–sea interaction, and material circulation in the upper ocean. Finally, these processes can occur in the atmosphere, ocean surface (wind waves and vortices), and fluids in general.

Remaining issues of this study include those related to unstable anticyclonic, baroclinic, and multiple vortices, and the shape, frequency, and amplitude of internal waves. As only stable cyclonic vortices are examined here; unstable and/or anticyclonic vortices need further investigation for the case $\delta > 0.15$. Regarding the baroclinic vortices, the interaction involves processes that are not considered here; for example, refraction and scattering by vertical shear, passage under a vortex concentrated in the upper layer, effects of advection of vertical displacement associated with vortices by wave velocity, and the effects of vertical advection. Preliminary experiments suggest that the interactions described in this study occur with one or more of the aforementioned effects. In the case of multiple vortices, the effects of the deformation field on the vortices should be considered.

Only sinusoidal waves are examined here, but beams and solitons are also important in the oceans. Regarding wind-induced near-inertial waves, δ is not estimated and scaling and interactions could be different, particularly for waves with zero horizontal wavenumber. To quantify the dissipation rate or diffusivity caused by the interactions investigated here, an estimate of δ is not sufficient; incoming wave energy is also needed. Further, the estimation of δ can be influenced by the wind, which disturbs the surface flow, and by numerical diffusion or dispersion, which strengthens with decreasing vortex size. These issues are left for future work.

Acknowledgments. This work was supported by JSPS KAKENHI (16H01587, 16K05549, 17H01156, 26247076, 21K03655), a 2019 ILTS leadership research grant, JHPCN (13-NA27, jh140046-NA26, jh150049-NA27, jh160060-NAJ, and jh170027-NAJ), and Hokkaido University IIC Next-Generation Supercomputer Programming Support 2019. We thank the reviewers for their useful comments. We thank Editage for English language editing.

Data availability statement. The numerical model used in this study is available from Dr. Yoshimasa Matsumura (ymatsu@aori.u-tokyo.ac.jp) at Atmosphere and Ocean Research Institute, the University of Tokyo. OFES30 output is available from Dr. Hideharu Sasaki (sasaki@jamstec.go.jp) at Application Laboratory, Japan Agency for Marine-Earth Science and Technology (JAMSTEC).

REFERENCES

Alford, M. H., 2003: Redistribution of energy available for ocean mixing by long-range propagation of internal waves. *Nature*, **423**, 159–162, https://doi.org/10.1038/nature01628.

Ansong, J. K., B. K. Arbic, M. C. Buijsman, J. G. Richman, J. F. Shriver, and A. J. Wallcraft, 2015: Indirect evidence for substantial damping of low-mode internal tides in the open ocean. *J. Geophys. Res. Oceans*, **120**, 6057–6071, https://doi.org/10.1002/2015JC010998.

Arbic, B. K., A. J. Wallcraft, and E. J. Metzger, 2010: Concurrent simulation of the eddying general circulation and tides in a global ocean model. *Ocean Modell.*, **32**, 175–187, https://doi.org/10.1016/j.ocemod.2010.01.007.

——, J. G. Richman, J. F. Shriver, P. G. Timko, E. J. Metzger, and A. J. Wallcraft, 2012: Global modeling of internal tides within an eddying ocean general circulation model. *Oceanography*, **25**, 20–29, https://doi.org/10.5670/oceanog.2012.38.

Badulin, S. I., and V. I. Shrira, 1993: On the irreversibility of internal-wave dynamics due to wave trapping by mean flow inhomogeneities. Part 1. Local analysis. *J. Fluid Mech.*, **251**, 21–53, https://doi.org/10.1017/S0022112093003325.

Bartello, P., 1995: Geostrophic adjustment and inverse cascades in rotating stratified turbulence. *J. Atmos. Sci.*, **52**, 4410–4428, https://doi.org/10.1175/1520-0469(1995)052<4410:GAAICI>2.0.CO;2.

Brunner-Suzuki, A.-M. E. G., M. A. Sundermeyer, and M.-P. Lelong, 2012: Vortex stability in a large-scale internal wave shear. *J. Phys. Oceanogr.*, **42**, 1668–1683, https://doi.org/10.1175/JPO-D-11-0137.1.

——, ——, and ——, 2014: Upscale energy transfer by the vortical mode and internal waves. *J. Phys. Oceanogr.*, **44**, 2446–2469, https://doi.org/10.1175/JPO-D-12-0149.1.

Bühler, O., 2014: *Waves and Mean Flows*. 2nd ed. Cambridge University Press, 374 pp.

——, and M. E. McIntyre, 1998: On non-dissipative wave-mean interactions in the atmosphere or oceans. *J. Fluid Mech.*, **354**, 301–343, https://doi.org/10.1017/S002211209700774X.

——, and ——, 2005: Wave capture and wave-vortex duality. *J. Fluid Mech.*, **534**, 67–95, https://doi.org/10.1017/S0022112005004374.

Calil, P. H. R., K. J. Richards, Y. Jia, and R. R. Bidigare, 2008: Eddy activity in the lee of the Hawaiian Islands. *Deep-Sea Res. II*, **55**, 1179–1194, https://doi.org/10.1016/j.dsr2.2008.01.008.

Chavanne, C., P. Flament, D. Luther, and K.-W. Gurgel, 2010: The surface expression of semidiurnal internal tides near a strong source at Hawaii. Part II: Interactions with mesoscale currents. *J. Phys. Oceanogr.*, **40**, 1180–1200, https://doi.org/10.1175/2010JPO4223.1.

Chelton, D. B., M. G. Schlax, and R. M. Samelson, 2011: Global observations of nonlinear mesoscale eddies. *Prog. Oceanogr.*, **91**, 167–216, https://doi.org/10.1016/j.pocean.2011.01.002.

Danioux, E., and J. Vanneste, 2016: Near-inertial-wave scattering by random flows. *Phys. Rev. Fluids*, **1**, 033701, https://doi.org/10.1103/PhysRevFluids.1.033701.

de Lavergne, C., and Coauthors, 2020: A parameterization of local and remote tidal mixing. *J. Adv. Model. Earth Syst.*, **12**, e2020MS002065, https://doi.org/10.1029/2020MS002065.

Dewar, W. K., and P. D. Killworth, 1995: On the stability of oceanic rings. *J. Phys. Oceanogr.*, **25**, 1467–1487, https://doi.org/10.1175/1520-0485(1995)025<1467:OTSOOR>2.0.CO;2.

Dong, B., and K. C. Yeh, 1988: Resonant and nonresonant wave-wave interactions in an isothermal atmosphere. *J. Geophys. Res.*, **93**, 3729–3744, https://doi.org/10.1029/JD093iD04p03729.

Dong, W., O. Bühler, and K. S. Smith, 2020: Frequency diffusion of waves by unsteady flows. *J. Fluid Mech.*, **905**, R3, https://doi.org/10.1017/jfm.2020.837.

Duda, T. F., Y.-T. Lin, M. Buijsman, and A. E. Newhall, 2018: Internal tidal modal ray refraction and energy ducting in baroclinic Gulf Stream currents. *J. Phys. Oceanogr.*, **48**, 1969–1993, https://doi.org/10.1175/JPO-D-18-0031.1.

Dunphy, M., and K. G. Lamb, 2014: Focusing and vertical mode scattering of the first mode internal tide by mesoscale eddy interaction. *J. Geophys. Res. Oceans*, **119**, 523–536, https://doi.org/10.1002/2013JC009293.

——, A. L. Ponte, P. Klein, and S. Le Gentil, 2017: Low-mode internal tide propagation in a turbulent eddy field. *J. Phys. Oceanogr.*, **47**, 649–665, https://doi.org/10.1175/JPO-D-16-0099.1.

Farge, M., and R. Sadourny, 1989: Wave-vortex dynamics in rotating shallow water. *J. Fluid Mech.*, **206**, 433–462, https://doi.org/10.1017/S0022112089002351.

Fu, L.-L., and R. Ferrari, 2008: Observing oceanic submesoscale processes from space. *Eos, Trans. Amer. Geophys. Union*, **89**, 488, https://doi.org/10.1029/2008EO480003.

Godoy-Diana, R., J.-M. Chomaz, and C. Donnadieu, 2006: Internal gravity waves in a dipolar wind: A wave-vortex interaction experiment in a stratified fluid. *J. Fluid Mech.*, **548**, 281–308, https://doi.org/10.1017/S0022112005007536.

Hoskins, B. J., I. Draghici, and H. C. Davies, 1978: A new look at the ω-equation. *Quart. J. Roy. Meteor. Soc.*, **104**, 31–38, https://doi.org/10.1002/qj.49710443903.

Huang, X., Z. Wang, Z. Zhang, Y. Yang, C. Zhou, Q. Yang, W. Zhao, and J. Tian, 2018: Role of mesoscale eddies in modulating the semidiurnal internal tide: Observation results in the northern South China Sea. *J. Phys. Oceanogr.*, **48**, 1749–1770, https://doi.org/10.1175/JPO-D-17-0209.1.

Jones, W. L., 1969: Ray tracing for internal gravity waves. *J. Geophys. Res.*, **74**, 2028–2033, https://doi.org/10.1029/JB074i008p02028.

Kafiabad, H. A., M. A. C. Savva, and J. Vanneste, 2019: Diffusion of inertia-gravity waves by geostrophic turbulence. *J. Fluid Mech.*, **869**, R7, https://doi.org/10.1017/jfm.2019.300.

——, J. Vanneste, and W. R. Young, 2021: Interaction of near-inertial waves with an anticyclonic vortex. *J. Phys. Oceanogr.*, **51**, 2035–2048, https://doi.org/10.1175/JPO-D-20-0257.1.

Kelly, S. M., P. F. J. Lermusiaux, T. F. Duda, and P. J. Haley Jr., 2016: A coupled-mode shallow-water model for tidal analysis: Internal tide reflection and refraction by the Gulf Stream. *J. Phys. Oceanogr.*, **46**, 3661–3679, https://doi.org/10.1175/JPO-D-16-0018.1.

Kerry, C. G., B. S. Powell, and G. S. Carter, 2014: The impact of subtidal circulation on internal-tide-induced mixing in the Philippine Sea. *J. Phys. Oceanogr.*, **44**, 3209–3224, https://doi.org/10.1175/JPO-D-13-0249.1.

Klein, P., and S. L. Smith, 2001: Horizontal dispersion of near-inertial oscillations in a turbulent mesoscale eddy field. *J. Mar. Res.*, **59**, 697–723, https://doi.org/10.1357/002224001762674908.

Klymak, J. M., R. Pinkel, and L. Rainville, 2008: Direct breaking of the internal tide near topography: Kaena Ridge, Hawaii. *J. Phys. Oceanogr.*, **38**, 380–399, https://doi.org/10.1175/2007JPO3728.1.

Kunze, E., 1985: Near-inertial wave propagation in geostrophic shear. *J. Phys. Oceanogr.*, **15**, 544–565, https://doi.org/10.1175/1520-0485(1985)015<0544:NIWPIG>2.0.CO;2.

——, and E. Boss, 1998: A model for vortex-trapped internal waves. *J. Phys. Oceanogr.*, **28**, 2104–2115, https://doi.org/10.1175/1520-0485(1998)028<2104:AMFVTI>2.0.CO;2.

Kuo, A. C., and L. M. Polvani, 1999: Wave-vortex interaction in rotating shallow water. Part 1. One space dimension. *J. Fluid Mech.*, **394**, 1–27, https://doi.org/10.1017/S0022112099005534.

Leith, C. E., 1980: Nonlinear normal mode initialization and quasi-geostrophic theory. *J. Atmos. Sci.*, **37**, 958–968, https://doi.org/10.1175/1520-0469(1980)037<0958:NNMIAQ>2.0.CO;2.

Lelong, M.-P., and J. J. Riley, 1991: Internal wave—Vortical mode interactions in strongly stratified flows. *J. Fluid Mech.*, **232**, 1–19, https://doi.org/10.1017/S0022112091003609.

——, Y. Cuypers, and P. Bouruet-Aubertot, 2020: Near-inertial energy propagation inside a Mediterranean anticyclonic eddy. *J. Phys. Oceanogr.*, **50**, 2271–2288, https://doi.org/10.1175/JPO-D-19-0211.1.

Liu, L., L. Ran, and S. Gao, 2019: A three-dimensional wave activity flux of inertia–gravity waves and its application to a rainstorm event. *Adv. Atmos. Sci.*, **36**, 206–218, https://doi.org/10.1007/s00376-018-8018-5.

MacKinnon, J. A., and Coauthors, 2017: Climate process team on internal wave-driven ocean mixing. *Bull. Amer. Meteor. Soc.*, **98**, 2429–2454, https://doi.org/10.1175/BAMS-D-16-0030.1.

Matsumura, Y., and H. Hasumi, 2008: A non-hydrostatic ocean model with a scalable multigrid Poisson solver. *Ocean Modell.*, **24**, 15–28, https://doi.org/10.1016/j.ocemod.2008.05.001.

Moulin, F. Y., and J. B. Flór, 2005: Experimental study on wave breaking and mixing properties in the periphery of an intense vortex. *Dyn. Atmos. Oceans*, **40**, 115–130, https://doi.org/10.1016/j.dynatmoce.2004.10.007.

Müller, P., and N. Xu, 1992: Scattering of oceanic internal gravity waves off random bottom topography. *J. Phys. Oceanogr.*, **22**, 474–488, https://doi.org/10.1175/1520-0485(1992)022<0474:SOOIGW>2.0.CO;2.

Nakamura, T., and T. Awaji, 2009: Scattering of internal waves with frequency change over rough topography. *J. Phys. Oceanogr.*, **39**, 1574–1594, https://doi.org/10.1175/2008JPO3795.1.

——, Y. Isoda, H. Mitsudera, S. Takagi, and M. Nagasawa, 2010: Breaking of unsteady lee waves generated by diurnal tides. *Geophys. Res. Lett.*, **37**, L04602, https://doi.org/10.1029/2009GL041456.

——, J. P. Matthews, T. Awaji, and H. Mitsudera, 2012: Submesoscale eddies near the Kuril straits: Asymmetric generation of clockwise and counterclockwise eddies by barotropic tidal flow. *J. Geophys. Res.*, **117**, C12014, https://doi.org/10.1029/2011JC007754.

Nikurashin, M., and R. Ferrari, 2011: Global energy conversion rate from geostrophic flows into internal lee waves in the deep ocean. *Geophys. Res. Lett.*, **38**, L08610, https://doi.org/10.1029/2011GL046576.

Okubo, A., 1970: Horizontal dispersion of floatable particles in the vicinity of velocity singularities such as convergences. *Deep-Sea Res. Oceanogr. Abstr.*, **17**, 445–454, https://doi.org/10.1016/0011-7471(70)90059-8.

Polzin, K. L., 2008: Mesoscale eddy-internal wave coupling. Part I: Symmetry, wave capture, and results from the mid-ocean dynamics experiment. *J. Phys. Oceanogr.*, **38**, 2556–2574, https://doi.org/10.1175/2008JPO3666.1.

——, 2010: Mesoscale eddy-internal wave coupling. Part II: Energetics and results from polymode. *J. Phys. Oceanogr.*, **40**, 789–801, https://doi.org/10.1175/2009JPO4039.1.

——, J. M. Toole, J. R. Ledwell, and R. W. Schmitt, 1997: Spatial variability of turbulent mixing in the abyssal ocean. *Science*, **276**, 93–96, https://doi.org/10.1126/science.276.5309.93.

Ponte, A. L., and P. Klein, 2015: Incoherent signature of internal tides on sea level in idealized numerical simulations. *Geophys. Res. Lett.*, **42**, 1520–1526, https://doi.org/10.1002/2014GL062583.

Rainville, L., and R. Pinkel, 2006: Baroclinic energy flux at the Hawaiian Ridge: Observations from the R/P FLIP. *J. Phys. Oceanogr.*, **36**, 1104–1122, https://doi.org/10.1175/JPO2882.1.

Ray, R. D., and G. T. Mitchum, 1997: Surface manifestation of internal tides in the deep ocean: Observations from altimetry and island gauges. *Prog. Oceanogr.*, **40**, 135–162, https://doi.org/10.1016/S0079-6611(97)00025-6.

——, and D. E. Cartwright, 2001: Estimates of internal tide energy fluxes from Topex/Poseidon altimetry: Central North Pacific. *Geophys. Res. Lett.*, **28**, 1259–1262, https://doi.org/10.1029/2000GL012447.

——, and E. D. Zaron, 2011: Non-stationary internal tides observed with satellite altimetry. *Geophys. Res. Lett.*, **38**, L17609, https://doi.org/10.1029/2011GL048617.

Rudnick, D. L., and Coauthors, 2003: From tides to mixing along the Hawaiian Ridge. *Science*, **301**, 355–357, https://doi.org/10.1126/science.1085837.

Salmon, R., 2016: Variational treatment of inertia-gravity waves interacting with a quasi-geostrophic mean flow. *J. Fluid Mech.*, **809**, 502–529, https://doi.org/10.1017/jfm.2016.693.

Sasaki, H., and P. Klein, 2012: SSH wavenumber spectra in the North Pacific from a high-resolution: Realistic simulation. *J. Phys. Oceanogr.*, **42**, 1233–1241, https://doi.org/10.1175/JPO-D-11-0180.1.

——, ——, B. Qiu, and Y. Sasai, 2014: Impact of oceanic-scale interactions on the seasonal modulation of ocean dynamics by the atmosphere. *Nat. Commun.*, **5**, 5636, https://doi.org/10.1038/ncomms6636.

——, ——, Y. Sasai, and B. Qiu, 2017: Regionality and seasonality of submesoscale and mesoscale turbulence in the North Pacific Ocean. *Ocean Dyn.*, **67**, 1195–1216, https://doi.org/10.1007/s10236-017-1083-y.

Savva, M. A. C., and J. Vanneste, 2018: Scattering of internal tides by barotropic quasigeostrophic flows. *J. Fluid Mech.*, **856**, 504–530, https://doi.org/10.1017/jfm.2018.694.

——, H. A. Kafiabad, and J. Vanneste, 2021: Inertia-gravity-wave scattering by three-dimensional geostrophic turbulence. *J. Fluid Mech.*, **916**, A6, https://doi.org/10.1017/jfm.2021.205.

Shriver, J. F., J. G. Richman, and B. K. Arbic, 2014: How stationary are the internal tides in a high-resolution global ocean circulation model? *J. Geophys. Res. Oceans*, **119**, 2769–2787, https://doi.org/10.1002/2013JC009423.

Smith, S. G. L., 1999: Near-inertial oscillations of a barotropic vortex: Trapped modes and time evolution. *J. Phys. Oceanogr.*, **29**, 747–761, https://doi.org/10.1175/1520-0485(1999)029<0747:NIOOAB>2.0.CO;2.

St. Laurent, L. C., H. L. Simmons, and S. R. Jayne, 2002: Estimating tidally driven mixing in the deep ocean. *Geophys. Res. Lett.*, **29**, 2106, https://doi.org/10.1029/2002GL015633.

Uematsu, A., R. Nakamura, Y. Nakajima, and Y. Yajima, 2013: X-band interferometric SAR sensor for the Japanese altimetry mission, COMPIRA. *2013 IEEE Int. Geoscience and Remote Sensing Symp.*, Melbourne, Victoria, Australia, Institute of Electrical and Electronics Engineers, 2943–2946, https://doi.org/10.1109/IGARSS.2013.6723442.

Wagner, G. L., and W. R. Young, 2015: Available potential vorticity and wave-averaged quasi-geostrophic flow. *J. Fluid Mech.*, **785**, 401–424, https://doi.org/10.1017/jfm.2015.626.

——, G. Ferrando, and W. R. Young, 2017: An asymptotic model for the propagation of oceanic internal tides through quasi-geostrophic flow. *J. Fluid Mech.*, **828**, 779–811, https://doi.org/10.1017/jfm.2017.509.

Ward, M. L., and W. K. Dewar, 2010: Scattering of gravity waves by potential vorticity in a shallow-water fluid. *J. Fluid Mech.*, **663**, 478–506, https://doi.org/10.1017/S0022112010003721.

Warn, B. T., 1986: Statistical mechanical equilibria of the shallow water equations. *Tellus*, **38A** (1), 1–11, https://doi.org/10.3402/tellusa.v38i1.11693.

Weiss, J., 1991: The dynamics of enstrophy transfer in two-dimensional hydrodynamics. *Physica D*, **48**, 273–294, https://doi.org/10.1016/0167-2789(91)90088-Q.

Whalen, C. B., 2021: Best practices for comparing ocean turbulence measurements across spatiotemporal scales. *J. Atmos. Oceanic Technol.*, **38**, 837–841, https://doi.org/10.1175/JTECH-D-20-0175.1.

——, J. A. MacKinnon, and L. D. Talley, 2018: Large-scale impacts of the mesoscale environment on mixing from wind-

driven internal waves. *Nat. Geosci.*, **11**, 842–847, https://doi.org/10.1038/s41561-018-0213-6.

Xie, J.-H., and J. Vanneste, 2015: A generalised-Lagrangian-mean model of the interactions between near-inertial waves and mean flow. *J. Fluid Mech.*, **774**, 143–169, https://doi.org/10.1017/jfm.2015.251.

Young, W. R., and M. Ben-Jelloul, 1997: Propagation of near-inertial oscillations through a geostrophic flow. *J. Mar. Res.*, **55**, 735–766, https://doi.org/10.1357/0022240973224283.

Zaron, E. D., and G. D. Egbert, 2014: Time-variable refraction of the internal tide at the Hawaiian Ridge. *J. Phys. Oceanogr.*, **44**, 538–557, https://doi.org/10.1175/JPO-D-12-0238.1.